PCCP

PERSPECTIVE

View Article Online
View Journal | View Issue

Cite this: Phys. Chem. Chem. Phys., 2015, 17, 2960

Review of one-dimensional and two-dimensional nanostructured materials for hydrogen generation

Veluru Jagadeesh Babu,†*[a] Sesha Vempati,†*[a] Tamer Uyar*[ab] and Seeram Ramakrishna*[c]

Received 22nd September 2014,
Accepted 28th November 2014

DOI: 10.1039/c4cp04245j

www.rsc.org/pccp

Hydrogen is an attractive alternative to fossil fuels in terms of environmental and other advantages. Of the various production methods for H_2, photocatalysis requires further development so that it can be applied economically on an industrial scale. One- and two-dimensional nanostructures in both pristine and modified forms have shown great potential as catalysts in the generation of H_2. We review here recent developments in these nanostructure catalysts and their efficiency in the generation of H_2 under UV/visible/simulated solar light. Despite much research effort, many photocatalysts do not yet meet the practical requirements for the generation of H_2, such as visible light activity. H_2 production is dependent on a variety of parameters and factors. To meet future energy demands, several challenges in H_2 production still need to be solved. We address here the factors that influence the efficiency of H_2 production and suggest alternatives. The nanostructures are classified based on their morphology and their efficiency is considered with respect to the influencing parameters. We suggest effective ways of engineering catalyst combinations to overcome the current performance barriers.

1. Introduction

Hydrogen (H_2) is considered to be an ideal fuel for future energy demands when it is sourced from clean and renewable energy resources.[1] H_2 has attracted much interest as a result of its potentially unlimited generation from the Earth's abundant water resources. On combustion, H_2 generates water rather than CO_2, in contrast to conventional fossil fuels. Its gravimetric energy content (heat of combustion) is about five times higher than that of methanol and ethanol and about 2.5 times that of hydrocarbons.[2] The greatest disadvantage of this fuel is its lack of natural availability. However, H_2 can be produced from both renewable and conventional energy sources (solar, wind, hydro and geothermal power, fossil fuels, nuclear energy and biomass sources[3]) (Fig. 1). Renewable energy currently contributes almost 5% of the overall hydrogen production through the electrolysis of water, whereas the rest is mainly derived from fossil fuels.[4] Producing H_2 from fossil fuels is not economically feasible because it requires a high temperature input for synthesis and emits CO_2; in addition, fossil fuels are non-renewable.[3] Thus the generation of H_2 from fossil fuels is not an environmentally friendly option.[5]

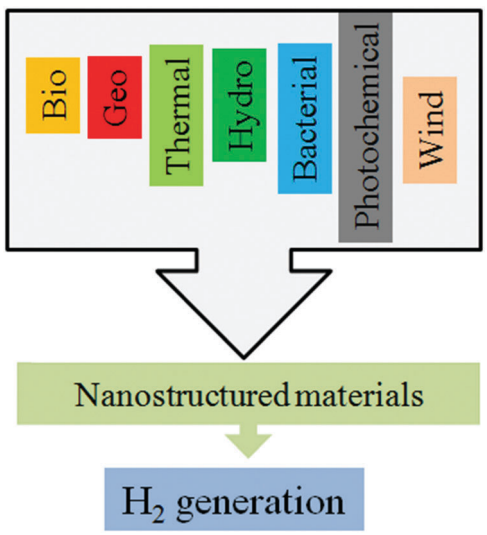

Fig. 1 Schematic diagram showing the various resources available for the production of H_2.

Among the renewable power sources, the photocatalytic splitting of water offers a promising method for the clean, low cost and environmentally friendly production of H_2 by solar energy. Nanostructured catalysts have additional advantages in

[a] UNAM-National Nanotechnology Research Center, Bilkent University, Ankara-06800, Turkey. E-mail: vjbabu2002@gmail.com, svempati01@qub.ac.uk
[b] Institute of Materials Science & Nanotechnology, Bilkent University, Ankara, 06800, Turkey. E-mail: uyar@unam.bilkent.edu.tr; Fax: +90 (312) 290 4365; Tel: +90 (312) 290 3571
[c] NUS Center for Nanofibers and Nanotechnology (NUSCNN), NUS Nanoscience and Nanotechnology Initiative (NUSNNI), National University of Singapore, Singapore-117576. E-mail: seeram@nus.edu.sg
† Authors contributed equally.

photocatalysis[6–11] and the photocatalytic production of H_2 from water *via* solar energy is currently the best available method and is an attractive and competitive technology. As technology advances, the implementation and associated costs of this technique will be significantly reduced. In 1972, Fujishima and Honda[12] demonstrated a photoelectrochemical (PEC) method to split water into H_2 and O_2 in which a bias was applied across a TiO_2 thin film and a Pt counter electrode. In 1979, Bard[13–15] showed that water can be split into H_2 and O_2 by simply using a powdered TiO_2 catalyst and exposing it to sunlight in the presence of a sacrificial reagent (SR) without applying any bias.

It is now understood that catalysis takes place on the surface of a semiconductor. When a photon of energy matches or exceeds the band gap energy (E_g) of a semiconductor, an electron is promoted to the conduction band (CB), leaving a hole in the valence band (VB). Essentially, the excited state CB electron and the VB hole can recombine or become trapped in a metastable surface state. They can also participate in reactions with electron donors and acceptors adsorbed on the surface of the semiconductor. Under suitable conditions, the CB electron can reduce H^+ ions to yield H_2 gas and the VB hole can generate O_2. Back-reactions to form H_2O instead of H_2 gas are possible.

Efficient e–h pair separation is crucial in catalysis. Selecting a semiconductor requires prior knowledge about the CB and VB levels with respect to the redox potential of H_2O, *i.e.* the CB should be lower than the H^+/H_2 potential and the VB should be higher than the OH^-/O_2 potential. The next immediate consideration is the E_g of the semiconductor, which determines the range of wavelengths for which it can absorb energy to create e–h pairs. Low E_g materials such as ferrous oxide (1.9–2.1 eV),[19] tungsten nitride (2.2 eV)[20] and other III–V and II–VI compound semiconductors[21–23] may be active materials within the limits of the energetic locations of the CB and VB with respect to the H_2O redox potential. For some semiconductors, although their E_g values cover the visible part of the solar spectrum, their CB and/or VB levels are not compatible with respect to the redox potential of H_2O. These materials, *e.g.* MoS_2, Fe_2O_3 and WO_3, may be photocorrosive if their CB minimum is lower than the thermodynamic requirement.[24] Such photocorrosive catalysts have been explored after certain modifications, such as the incorporation of co-catalysts (NiO_x, RuO_2[25,26] or Rh–Cr), doping with metal ions or combination with other semiconductors.[5,27–29] The same principle of thermodynamic requirement applies to the PEC method.[29,30]

Considerable use of small E_g semiconducting materials may cause serious environmental impacts as a result of their instability; wide E_g materials are preferable in H_2 production. However, although suitable band positions and stability in the electrolyte favour large E_g materials (*e.g.* TiO_2 or ZnO),[30–32] their absorbance is limited to the UV region of the solar spectrum. A significant solar-to-hydrogen conversion efficiency (η) of 16.25% has been obtained from TiO_2 nanotubes (NTs) (45 μm) under 100 mW cm^{-2} irradiation with UV light (320–400 nm).[33] Only a small fraction (about 5%) of the available energy in the solar spectrum is used in this example. Wide E_g materials can be subjected to modifications, such as doping[34] and interfacing with other materials[35,36] in the form of heterojunctions, to enable absorption in the visible region or to efficiently isolate the e–h pairs. This offers a clean, cost-effective and environmentally benign production method for H_2. Izumi *et al.*[34] studied the visible light response over TiO_2 NTs by anionic (S, N) doping. Zhan *et al.*[35] demonstrated that this heterostructure can cover about 22% of the entire solar spectrum. Sathre *et al.*[37] analysed the PEC method of hydrogen production based on fundamental principles. Hisatomi *et al.*[38] addressed the fundamental aspects of the PEC method of water splitting. The Z-scheme and tandem systems based on multi-step photoexcitation liberate semiconducting materials from thermodynamic limitations and enable the application of a variety of materials to unassisted water splitting.[38]

Semiconducting nanostructures, especially one-dimensional (1D) and two-dimensional (2D) structures have superior photocatalytic activity as a result of improved e–h separation and a low recombination rate. Ford *et al.*[16] reported that, by decreasing the diameters of InAs nanowires (NWs), the mobility of the electrons could be controlled. Martinson *et al.*[17] compared the transport and recombination dynamics of sintered nanocrystalline particles *versus* nanorod (NR) arrays. Core–shell type nanostructures[18] have been demonstrated to have enhanced PEC water splitting properties under solar light. Various architectures of 2D nanosheets (NSs) with thicknesses <100 nm hold great promise for the efficient PEC splitting of water. 2D NSs also offer optimized charge migration, surface modification and light absorption. Zhou *et al.*[39] addressed the performance of advanced PEC devices using 2D NSs as photoelectrodes. Chemically modified nanostructures offer a green and low cost method of generating H_2 fuel *via* PEC water splitting.[40] Liu *et al.*[41] demonstrated that Pt-loaded titania hierarchical photonic crystals could double the evolution of H_2 in photocatalytic water splitting. The enhancement in H_2 evolution was a result of the hierarchical structure, which can cause multiple scattering among the photonic crystals and improve the absorbance of light. This provides a strong light-harvesting method.

The focus of research has recently intensified towards nanostructures and their potential applications. The high specific surface area (SA) of nanostructures provides a high density of active sites compared with their bulk counterparts.[42,43] The effect of quantum confinement results in important optical and electronic properties. The properties of various types of 1D and 2D semiconducting nanostructures, such as NRs, NWs, NTs and nanofibres (NFs)[44,45] are considered in the next section, against the background of H_2 generation.

1.1. Why nanostructures for H_2 generation?

The growing interest in nanostructured metal oxides[46–55] is due to their large SA, short lateral diffusion length and low reflectivity. However, most metal oxides have large band gap energies, leading to limited light absorption in the visible region. This imposes a fundamental limitation on the overall conversion efficiency of solar energy to hydrogen. Delaying the recombination of photogenerated e–h pairs creates the environment required for the exciton pair to diffuse to the surface and participate in catalysis. 1D nanostructures can trap photons more effectively

under appropriate geometric configurations where the carrier diffusion lengths are comparable with their physical dimensions.[46] As a result, the photocatalytic performance significantly increases[47–55] at smaller dimensions. The preparation of nanostructured photocatalysts is therefore indispensable in meeting future energy demands. The nano-dimensions facilitate the efficient collection of free carriers and increase η.[56–58]

This concept of charge carrier generation and subsequent migration is similar to that in solar cells, where the intrinsic electrical field assists the separation. This concept of using an intrinsic electrical field is applied in H_2 generation.[59] n–n type heterojunctions yield similar results.[35] In the case of photocatalytic H_2 generation, the migration should take place by itself, although some assistance may be obtained from the depletion layer (if it exists) on the surface. Arrays of NRs have attracted considerable interest as a result of their enhanced absorption of incident light and their crystallinity. For example, ZnO NR arrays,[60] single crystalline GaN NRs[61] and GaP NRs[62] can be used as effective anti-reflection coatings as a result of their regular textures and morphology. Strontium metaniobate ($SrNb_2O_6$) NT morphologies are effective photocatalysts compared with their micron-sized powders. However, single crystalline ZnO shows enhanced electron collection efficiency compared with polycrystalline ZnO nanostructures,[17] due to shorter collection times. Light reflection increases the ratio of non-diffusive absorption and diffusive scattering, which results in a reduction in photon harvesting.[63] The periodic nature of nanostructures and their intrinsic property of low reflectivity can also be seen with NWs. NW arrays have a higher theoretical absorbance at lower wavelength regions than their thin-film counterparts.[64] Single-crystal Si NWs have delayed recombination and high optical absorption.[43,65,66]

NW structures can absorb incident photons while the low-energy photons are scattered inside the structure. Further increase in absorbance can be obtained by tailoring the fill factor of NWs.[64] This phenomena of multiple reflections inside the nanostructure is similar to that seen in NT.[67] These 1D structures (NWs and NTs) act as electron pathways in the axial directions. However, the scattered or transmitted light has a higher wavelength, which requires the use of sensitizers such as dyes (*e.g.* Eosin Y[68] in combination with carbon NTs) to increase η. Arrays of NWs[69] and dual-diameter germanium nanopillars[70] have effective photon absorption at low (300–600 nm) and high (600–900 nm) wavelengths, respectively. Single crystalline TiO_2 NWs showed faster electron mobility (about 1 $cm^2\ V^{-1}\ s^{-1}$) than polycrystalline NWs;[71] likewise single crystalline ZnO NWs (1–5 $cm^2\ V^{-1}\ s^{-1}$).[72] Although the mobility of the charge carriers in 1D polycrystalline TiO_2 is comparable with that of zero-dimensional (0D) TiO_2,[67,73] the recombination time of 1D polycrystalline TiO_2 is much longer than that of 0D TiO_2. This may be a result of the unevenly distributed recombination centres on the surface. Furthermore, the radial electrical field that may be present in 1D NWs delays the recombination process, which accounts for the enhanced electron collection efficiency in 1D TiO_2.[73–75] 1D materials with relatively small E_g values have been reported to have η = 0.6% (branched CuO NWs) and η = 0.71% (CuO–ZnO core–shell NR arrays).[27] Hexagonal Zn_2GeO_4 NRs show the highest rate of H_2 evolution of 0.6 mmol h^{-1}.[76] A comparative study showed that Zn_2GeO_4 NRs could produce a stable rate of H_2 evolution of 6.24 mmol $g^{-1}\ h^{-1}$ under irradiation with UV light.[77]

Haematite (α-Fe_2O_3) was considered for PEC solar water splitting[78] with 3D nanophotonic structures, which resulted in a current density as high as 3.05 mA cm^{-2} at 1.23 V with respect to the reversible hydrogen electrode (RHE). Hwang *et al.*[79] reported that layered perovskites loaded with Ni are important photocatalysts for water splitting, with a photon yield of 23%. A quantum yield as high as 30% was obtained when $K_2La_2Ti_3O_{10}$ was prepared by a polymerized complex method.[80] Zhang *et al.*[81] reported an improved photochemical evolution of H_2 from a TiO_2 leaf structure. Nanostructures are therefore potential recyclable candidates for water splitting.[82] Analysis from the ISI Web of Science has shown extensive growth in research on H_2 production (Fig. 2). It is clear from Fig. 2 and 3 that PEC water splitting is a potentially important method of producing H_2 with environmentally friendly features. Fig. 3 suggests that nanostructured materials are promising PEC catalysts.

This review focuses on the fundamental properties of nanostructured materials and their efficiency in the context of

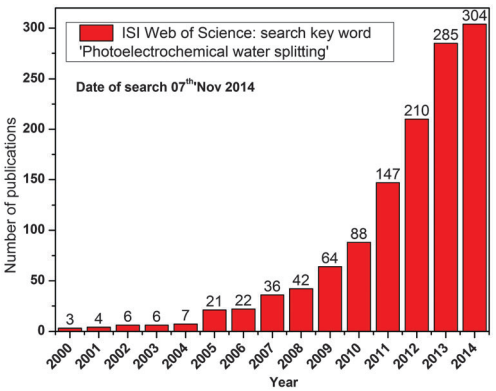

Fig. 2 Number of publications on PEC water splitting per year, 2000–2014.

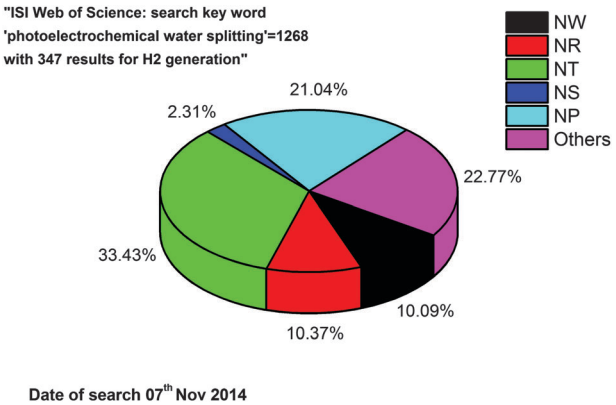

Fig. 3 H_2 evolution from various nanostructures *via* PEC water splitting. NW = nanowires, NR = nanorods, NT = nanotubes, NS = nanosheets, NP = nanoparticles. 'Others' includes nanofibres, nanolayers, nanoribbons and nanospheres.

processing parameters. The basic mechanism of H_2 evolution is addressed, including the vital points that influence the catalytic activity. A wide range of photocatalysts has been developed for use under UV illumination and have been modified to extend their capability to use visible light. H_2 evolution from various nanostructures are classified into two major sections: UV and visible illumination, along with various types of nanostructures such as NRs and NSs. The efficiencies and amount of H_2 evolution from various materials in different morphologies are tabulated separately for both the UV and visible regions. Important results and the relevant configurations (*e.g.* heterojunctions) are discussed in detail. In the concluding remarks, we consider the crucial points that require further attention in the design of the next generation of catalysts.

2. Basic mechanisms of hydrogen generation

The basic PEC setup[12] for water splitting is shown in Fig. 4a. When electrolysis takes place, the water molecules undergo redox reactions to generate H_2 and O_2 at the Pt and TiO_2 electrodes, respectively. This PEC setup was later simplified by Bard,[13–15] who used semiconducting particles and/or powders in the presence of aromatic compounds (Fig. 4b) as heterogeneous catalysts. The involvement of a semiconductor (catalyst), from which e–h pairs are photogenerated to then take part in catalysis, is essential. The crucial factor in enhancing the productivity is to delay the recombination of the excited e–h pairs and their subsequent migration (diffusion) to the surface. The output from the catalyst depends on how efficiently the e–h pairs are created and how well they diffuse to the surface.

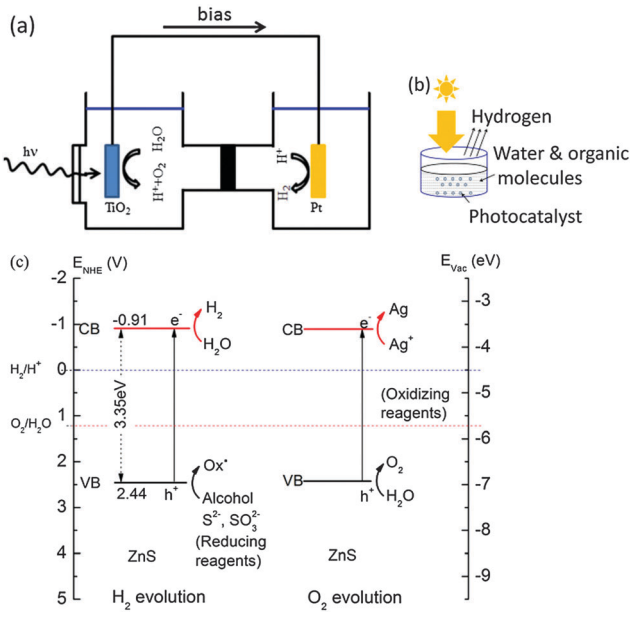

Fig. 4 Schematic diagrams of the setup for electrochemical water splitting: (a) after Fujishima and Honda;[12] (b) using powdered photocatalysts (after Bard[13–15]); and (c) basic principle of water splitting with photocatalyst materials (figure redrawn based on Kudo and Misekia[24]).

These factors depend on the semiconductor used,[16,17,60–62] the morphology,[16,60] the crystal structure,[17,25,61,62] intrinsic/surface defects, the intrinsic carrier lifetime and the collection time.[17] These factors can be tuned in nano-scale catalysts.

The mechanism of water splitting is as follows. The water molecules are reduced to form H_2 and oxidized to form O_2. The reduction and oxidation are mediated by electrons and holes, respectively. The redox potential of water is 1.23 V, *i.e.* H^+/H_2 is 0 V and O_2/H_2O is 1.23 V with respect to the normal hydrogen electrode (NHE) (Fig. 4c). Under suitable illumination, electrons and holes are created in the CB and VB, respectively. Several factors are involved in photocatalytic water splitting that finally determine the value of η. These are: (1) the absorption of photons to form excited e–h pairs; (2) the recombination, separation, migration, trapping and migration of excited charge carriers; and (3) surface chemical reactions (the construction of surface reaction active sites for the evolution of H_2 and O_2). When the conditions are favourable, these photoexcited electrons and holes migrate to the surface of the photocatalyst (Fig. 4). Fig. 4c describes the role of SRs in the catalysis process. As the quantity of SR decreases, the H_2 production rate also decreases; however, the production rate can be regained if the reagent is replenished.[83] It has been reported that SRs can effectively reduce H_2O to H_2 or oxide it to O_2. Co-catalysts and/or the addition of SRs to TiO_2 resulted in an improved performance.[24] A sufficiently negative flat band potential, a good absorption cross-section over a wide spectral range, photostability and an appropriate band gap are also essential. In this context, metal oxides such as TiO_2, $SrTiO_3$ and $NaTiO_3$ have been studied in detail as a result of their suitable band structures, low environmental impact and low toxicity, and high stability. However, these wide band gap oxides have only low conversion efficiencies as they are only active under UV light, which accounts for just 4% of the solar spectrum. Buhler *et al.*[84] reported that CdS has promising absorption up to 520 nm and has a flat band potential of −0.66 V (pH 7). However, the E_g of CdS is still relatively large (2.5 eV) and is not stable in aqueous solution under irradiation (anodic dissolution), although it can be stabilized in aqueous solutions by using reducing agents or SRs that provide electron donors to consume the photogenerated holes. SRs promote H_2 evolution by contributing to half of the reaction.[84] Where the SRs used two outputs can be expected: one is H_2, although and the second is desulfurization processes of S^{2-} and SO_3^{2-}. In the case of dye sensitization,[85] excitation and subsequent charge transfers occur on a sub-nanosecond or picosecond timescale. As electrons populate the CB, their energy should be more negative than H^+/H_2 with reference to the NHE. Holes participate in catalysis from the VB and their energy should be more positive than O_2/H_2O (1.23 V) with reference to the NHE. Therefore the E_g of the photocatalyst should be >1.23 eV. The energetic levels of the VB and CB play a vital part in water splitting, where their edges correspond to the ionization potential and electron affinity, respectively. Fig. 5 shows the CB and VB edges for various semiconductors with reference to the NHE and a vacuum; these values are also given in Table 1 for easy reference.

The basic half-equations which form H_2 and O_2 gases are given in eqn (1)–(3). As a result of the uphill nature of the

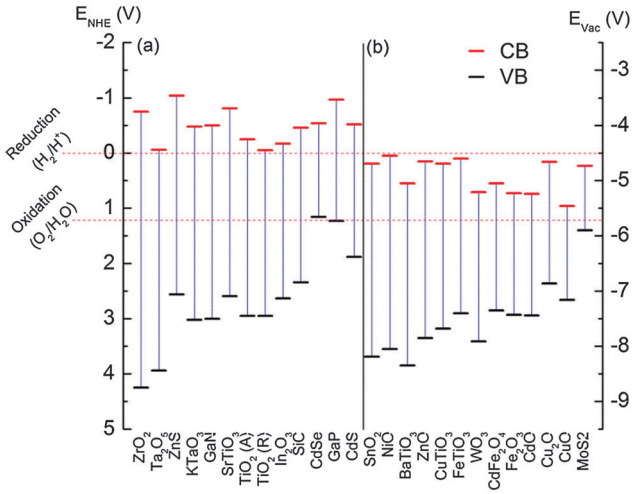

Fig. 5 Absolute CB and VB energy levels for some semiconducting photocatalysts with respect to the NHE and vacuum (Vac). Thermodynamically (a) suitable and (b) unsuitable materials. The band edge values for other perovskites are given in Castelli *et al.*[86]

Table 1 VB and CB levels of some semiconductors

	Band levels with respect to NHE (eV)			
Semiconductor	CB	VB	E_g	Ref.
ZrO_2	−0.75	4.25	5.0	87
Ta_2O5	−0.06	3.94	4.0	87
ZnS	−0.91	2.44	3.35	88
$KTaO_3$	−0.48	3.02	3.5	87
GaN	−0.5	3.0	3.5	89
$SrTiO_3$	−0.81	2.59	3.4	90
TiO_2 (A)	−0.25	2.95	3.2	90
TiO_2 (R)	−0.05	2.95	3.0	90
In_2O_3	−0.17	2.63	2.8	87
SiC	−0.46	2.34	2.8	91
CdSe	−0.54	1.16	1.7	24
GaP	−0.97	1.23	2.2	24
CdS	−0.52	1.88	2.4	87
SnO_2	0.19	3.69	3.5	87
NiO	0.05	3.55	3.5	87
$BaTiO_3$	0.55	3.85	3.3	87
ZnO	0.15	3.35	3.2	87
$CuTiO_3$	0.19	3.18	3.0	87
$FeTiO_3$	0.1	2.9	2.8	87
WO_3	0.71	3.41	2.7	87
$CdFe_2O_4$	0.55	2.85	2.3	87
Fe_2O_3	0.73	2.93	2.2	87
CdO	0.74	2.94	2.2	87
Cu_2O	0.16	2.36	2.2	87
CuO	0.96	2.66	1.7	87
MoS_2	0.23	1.4	1.2	87

reaction (positive change of Gibbs free energy $\Delta G^0 = 237$ kJ mol^{-1} at 25 °C), back-reactions may take place between H_2 and O_2 to form water in addition to intermediate products. Hence the surface of the catalyst or co-catalyst (if any) should be less supportive of the back-reactions.

$$\text{Reduction-Pt (Fig. 4c): } 2H^+ (aq) + 2e^- \rightarrow H_2 (g) \quad (1)$$

$$\text{Oxidation-catalyst (Fig. 4c): } 2H_2O (l) + 4h^+ \rightarrow O_2 (g) + 4H^+ \quad (2)$$

$$\text{Overall reaction: } 2H_2O (l) \rightarrow 2H_2 (g) + O_2 (g) \quad (3)$$

Fig. 5 gives information about semiconducting catalysts that are suitable and unsuitable materials for H_2 production. Fig. 5a shows that, for most of the semiconductors, the VB edge is deeper than the O_2/H_2O oxidation potential. Hence there is no need for a co-catalyst, except in special cases. To increase the value of η, the visible light region of the solar spectrum should be used. Although there are some semiconductors whose band gap covers the visible light region of solar spectrum, they are not considered as active materials because of their unsuitable band energies with respect to the NHE. These semiconductors (*e.g.* MoS_2, Fe_2O_3 and WO_3) are known to be photocorrosive materials as their CB minimum is lower than the thermodynamic requirement (Fig. 5b).[24] Wide band gap materials cannot harvest visible light, unless suitably modified. As an example, Fig. 6 shows a schematic band diagram of doped TiO_2.[34] Under UV illumination ($h\nu_1$), the evolution of both H_2 and O_2 is favourable. In the S-doped TiO_2, the evolution of O_2 is possible at S^{2-} sites under illumination with visible light ($h\nu_2$), *i.e.* the S^{2-} state lies above the O_2/H_2O oxidation potential. In contrast, for V-doped TiO_2, the evolution of H_2 is not possible at the $V^{4+/5+}$ site under illumination with visible light ($h\nu_3$), *i.e.* the $V^{4+/5+}$ state is at a higher potential than the H_2/H^+ reduction potential. It is important to note that the dopants form localized states. If they are accessible on the surface, then catalysis takes place from holes and electrons if the essential criteria for the redox potentials are met. Many photocatalysts have been reported to work under UV/visible light irradiation.[2]

Charge separation and migration of the photogenerated charge carriers are strongly affected by changes in crystal structure (polymorphs),[77,92] crystallinity[93] and particle size. Lattice defects act as traps or recombination centres and, consequently, the catalytic activity decreases. The density of defects can be lowered by increasing the crystallinity. By decreasing the size of the semiconductor, the photogenerated e–h pairs can migrate to the surface before they are trapped or recombined. If a catalytic site is

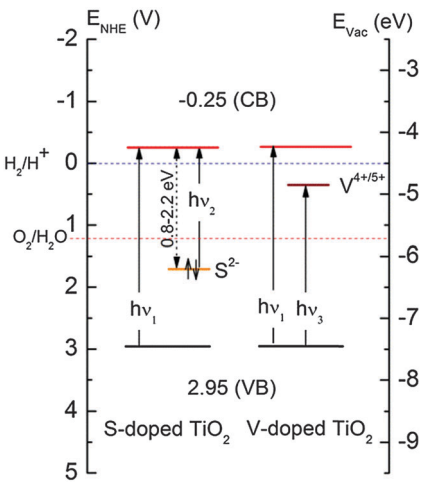

Fig. 6 Schematic band diagram for S- or V-doped TiO_2. Figure redrawn based on Izumi *et al.*[34]

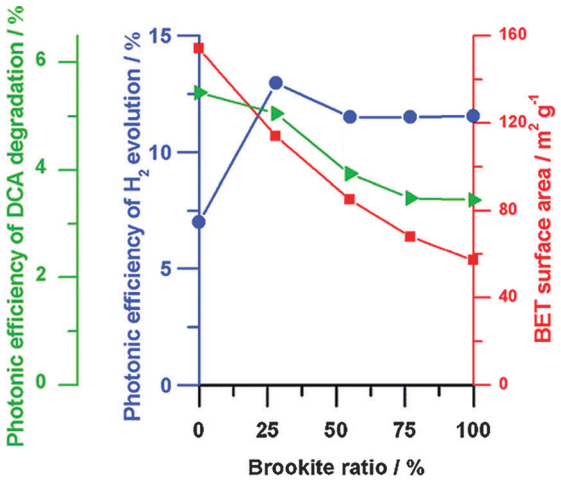

Fig. 7 Photonic efficiency and surface area *versus* the content of brookite. Green triangles = photonic efficiency of dichloroacetic acid (DCA) degradation; red squares = surface area; and blue circles = photonic efficiency of H_2 evolution. Conditions: catalyst, 0.5 g L^{-1}; aqueous 1 mM L^{-1} DCA, 60 mL; and pH 3. Reproduced with copyright permission from ref. 92.

not available even after reaching the surface, then they will have to recombine irrespective of whether they have a high enough potential to split water molecules. The surface chemical reactions depend on the SA and the density of surface defects.

Doped TiO_2 is visibly active where the dopants create intermediate bands within the band gap. However, the evolution of H_2 varies within TiO_2 polymorphs[92] (Fig. 7), in which the flat band potential of rutile and anatase varies with reference to the H^+ reduction potential. The flat band potential of rutile TiO_2 is almost the same as that of the reduction potential of protons, whereas that of anatase TiO_2 is shifted negatively by about 0.2 V.[94] This implies that the photogenerated electrons in anatase are more energetic than those in rutile. When recombination sites are dominant, as in amorphous TiO_2, negligible catalytic activity is expected.[95] Another polymorph of TiO_2 is brookite, which has a better catalytic activity than commercial TiO_2 (P-25).[96] Again, the difference in the flat band potential explains the higher efficiency: for brookite, the flat band potential is cathodically shifted by 0.14 V compared with anatase. Kandiel *et al.*[92] studied three TiO_2 polymorphs with respect to their production of H_2 from MeOH–H_2O gas. Their results suggested that the anatase and brookite phases result in similar H_2 production, whereas rutile has a lower performance. Cubic structured $KNbO_3$ had a higher rate of H_2 production than orthorhombic and commercial $KNbO_3$.[97]

3. Quantification of hydrogen generation

Many types of illumination sources (Xe or Hg lamps) have been used with different amounts of catalysts. An agreed quantification method is needed so that efficiencies can be compared across different studies.

3.1. Solar-to-hydrogen conversion efficiency (η,%)

The efficiency of H_2 generation can be measured either by quantifying the amount of H_2 gas evolved or the number of electrons transferred from the photocatalyst to the water within a certain time period under illumination. The overall conversion of solar energy is given by the following equation:[33]

$$(\%) = \frac{\text{total power output} - \text{electrical power output}}{\text{energy of incident light}} \times 100$$

$$= j_p\left[\left(E^0_{rev} - \left|E_{app}\right|\right)/I_0\right] \times 100 \quad (4)$$

where j_p is the photocurrent density (mW cm^{-2}), $j_pE^0_{rev}$ is the total power output, $j_p|E_{app}|$ is the electrical power output and I_0 is the power density of the incident light (mW cm^{-2}). E^0_{rev} is the standard reversible potential (1.23 V/NHE). E_{app} is the applied potential, which can be derived from $E_{app} = E_{meas} - E_{aoc}$, where E_{meas} is the electrode potential of the working electrode at which the photocurrent was measured under illumination and E_{aoc} is the electrode potential of the same working electrode under open circuit conditions, under the same illumination when immersed in the same electrolyte. E_{aoc} and E_{app} are measured with respect to Ag/AgCl. The voltage at which the photocurrent becomes zero is taken as E_{aoc}. The details of the light source can be included in the quantification process and the quantum yield (QY) can be calculated. The overall QY is defined in eqn (5) and (6) for H_2 and O_2, respectively:[98]

$$QY\% = \frac{2 \times \text{number of evolved } H_2 \text{ molecules}}{\text{number of absorbed photons}} \times 100 \quad (5)$$

$$QY\% = \frac{4 \times \text{number of evolved } O_2 \text{ molecules}}{\text{number of absorbed photons}} \times 100 \quad (6)$$

Some photocatalysts are active in visible light, whereas others are active in the UV region of the solar spectrum. Although the principle of H_2 generation is the same for both UV and visible irradiation, given the large amount of visible light available it is appropriate to discuss these regions separately.

4. UV-active nanostructured photocatalysts for hydrogen generation

Wide band gap semiconductors can only use the UV region of the solar spectrum. Nevertheless, considerable amounts of H_2 have been reported[47–52] to be produced when these catalysts are in the form of nanostructures.[5,99] The density of active surface sites increases with increasing SA,[100–102] particularly with 1D nanostructures, which have fast charge transfer rates and efficient charge separation.[103] For example, NWs,[93,104,105] NTs,[106–110] NRs/nanoribbons[111–116] and NFs[44,117–121] have shown great potential for the production of H_2. However, it is vital to understand which type of 1D structure is better for the generation of H_2. We have carried out a comparative analysis of these 1D structures with respect to their efficiency under UV irradiation.

4.1. Nanowires

NWs have shown significance photocatalytic activity as a result of the improvement in electron–hole separation and lower recombination rates. Such remarkable features are highly desirable to

enhance the efficiency of PEC water splitting. NWs have been studied extensively.[93,122–124] Yang *et al.*[122] reported that N-doped ZnO NWs used as photoanodes in PEC yielded relatively higher efficiencies as a result of the improved charge transport over the 0D nanostructures. TiO_2 NWs were more effective for H_2 generation than commercial TiO_2 nanoparticles (NPs). The yield from these NWs was about 1.421 μmol m^{-2}, which is significant[123] and was ascribed to the high SA and low recombination rate of the e–h pairs. Jitputti *et al.*[93] studied TiO_2 NWs with methanol as a SR to show the effects of post-treatment and its consequences for the SA. The SRs removed the photogenerated holes in an irreversible fashion, thereby preventing mutual electron–hole recombination and the H_2 and O_2 back-reaction[124] (eqn (2)). The overall process can be expressed by the following equations:[125]

$$CH_3OH \xrightarrow{h\nu,\,\mathrm{Cat.}} HCHO + H_2 \quad (7)$$

$$HCHO + H_2O \xrightarrow{h\nu,\,\mathrm{Cat.}} HCO_2H + H_2 \quad (8)$$

$$HCO_2H \xrightarrow{h\nu,\,\mathrm{Cat.}} CO_2 + H_2 \quad (9)$$

$$CO_2 + H_2O \xrightarrow{h\nu,\,(\mathrm{M-TiO_2})} \begin{cases} CH_4 \\ CH_2O \\ CH_3COOH \\ (\text{where } \mathrm{M} = \mathrm{Pt, Pd, Au, Cu, Ru}) \end{cases} \quad (10)$$

Notably, methanol is oxidized to form CO_2, which is an adverse effect. Despite this, the H_2 yield was about 20.1 μmol h^{-1} for the samples post-treated at 500 °C for 1 h (Fig. 8). This may be because the unique 1D NWs and high crystallinity promoted the evolution of H_2 under UV irradiation.[93] The amount of H_2 evolved increases with increasing post-treatment temperatures up to 500 °C, then decreases with further increases in temperature. The decrease may be a result of the lowered SA. A similar effect has been reported[26] for lithium niobate ($LiNbO_3$) NWs, for which a higher SA yielded better results. However, when RuO_2 is used as a co-catalyst under UV-visible illumination, the overall amount of water splitting is increased.

Si NWs (n type) are known for their competitive carrier recombination. Forming a p–n heterojunction accelerates improves the separation of the photogenerated charge carriers. This was illustrated by Xiong *et al.*[59] using Cu_2O (p-type) as a core–shell structure with Pt as a co-catalyst. This composite structure showed a nearly 45% increase in the generation of H_2 compared with pristine Si NWs. In addition to p–n type heterojunctions,[59] n–n type heterojunctions have also been investigated in a similar core–shell structure with ZnO/$Zn_xCd_{1-x}Te$ NWs.[35] To put this in context, it is important to mention a study[36] which showed the selective isolation of electron–hole pairs in an n–n type heterojunction. Such structures help to isolate the hole, thereby inhibiting back-reactions. In ZnO–$Zn_xCd_{1-x}Te$ NW heterojunctions, the shell material absorbs in the NIR

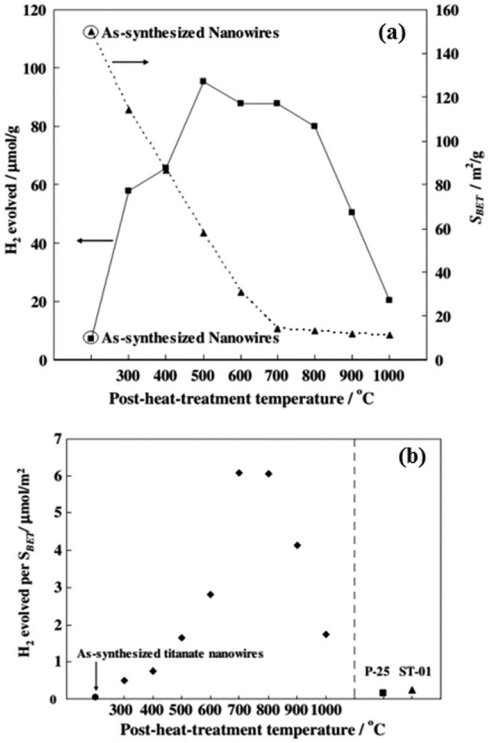

Fig. 8 Efficiency of H_2 generation at different post-treatment temperatures with respect to (a) surface area (S_{BET}) and (b) TiO_2 powder (Degussa P-25) and commercial TiO_2 (Ishihara ST-01). Reproduced with copyright permission from ref. 93.

region (855 nm), in contrast with the core, which absorbs the UV region (380 nm), covering about 22% of the solar spectrum. Under suitable illumination, type II band alignment allows the transfer of photogenerated electrons from the CB of $Zn_xCd_{1-x}Te$ (E_g tunability 2.25–1.45 eV depending on the Cd : Zn ratio) to the CB of ZnO (Fig. 9a). The recombination is delayed while the transfer takes place, yielding higher H_2 production. The electrons collected at the ITO produce H_2 molecules. The holes are transferred to the VB of the $Zn_xCd_{1-x}Te$ shell and are consumed by the SR (S^{2-} and SO_3^{2-}). If the $Zn_xCd_{1-x}Te$ covers the whole substrate, including the ITO, then it is not useful for the generation of H_2. As the ITO is an expensive substrate, alternative methods of fabrication should be considered. For example, if ZnO is taken as the shell and $Zn_xCd_{1-x}Te$ as the core, then the electrons can take part in the catalysis from a much higher SA (in the original configuration[35] it is just the ITO). Even if the ZnO covers the whole substrate, good access to the electrons is preserved when the fabrication difficulties in this configuration are acknowledged.

These heterojunctions have been developed further by introducing Pt as a co-catalyst[126] – for example, in CdSe–CdS core–shell NW heterojunctions. After charge generation the Pt acts as an electron collector and enhances the production of H_2 at its best value of 434.29 μmol h^{-1} g^{-1} under UV illumination. The CdS shell also helps to passivate the surface defects of the core, which helps to increase the carrier lifetime. Tongying *et al.*[126] illustrated a band diagram without considering the energetic

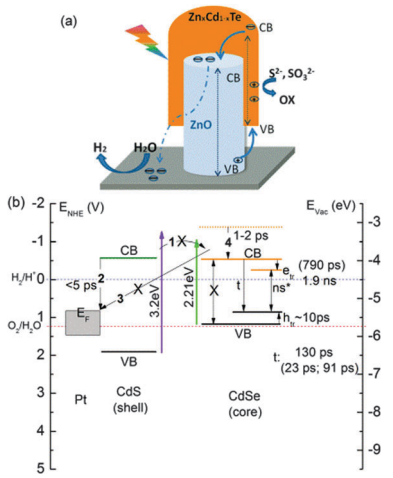

Fig. 9 (a) Schematic representation of the charge transfer and separation process in ZnO/$Zn_xCd_{1-x}Te$ core–shell NW array. Reproduced with copyright permission from ref. 35. (b) CdSe–CdS core–shell NW heterojunctions with Pt as the co-catalyst.[126] e_{tr} and h_{tr} are electron and hole traps, respectively.

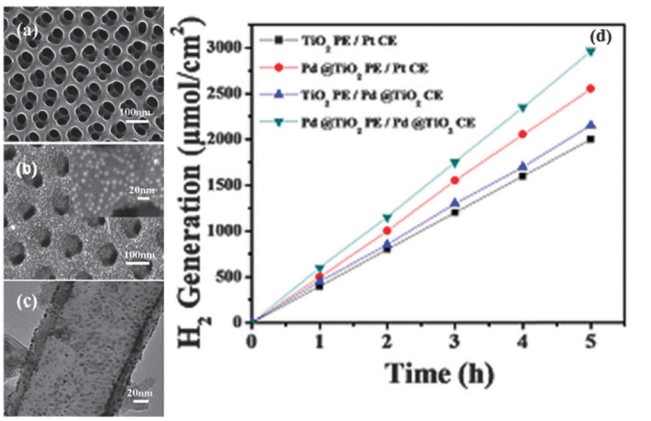

Fig. 10 SEM micrographs of (a) TiO_2 NTs and (b) TiO_2 NT coated with Pd QDs (inset shows higher magnification) (c) TEM image of TiO_2 NTs with Pd QDs. (d) H_2 generation from various catalysts plotted against time. Reproduced with the copyright permission from ref. 140.

locations of the bands. However, we have redrawn this (Fig. 9b), taking the CB and VB edges for the two semiconductors from Table 1. In process 1, Tongying *et al.*[126] suggested that the electron from the CB of CdS does not reach the CB of CdSe. In process 2, the electron from the CB of CdS takes <5 ps to reach the E_F of Pt. Process 3 is, of course, not possible given the physical inaccessibility. In process 4, the electron takes nearly 1–2 ps to reach the bottom of the CB of CdSe. Electron and hole trap processes (e_{tr} and h_{tr}, respectively) take place in CdSe and the time-scales are shown in Fig. 9b. Within CdSe it was suggested[126] that the electrons are not excited to the bottom of the CB and hence do not recombine directly, however mediated by e_{tr} and h_{tr}. Wu *et al.*[127] reported the evolution of H_2 from N-doped TiO_2 NFs (hydrothermal) decorated with Pt NPs of about 2 nm diameter under different wavelengths of illumination. The catalysts were effective in the production of H_2 with conversion efficiencies of 3.6 and 12.3% for UV irradiation at 365 and 312 nm, respectively.

4.2. Nanotubes

TiO_2-based NTs have been shown to have considerable efficiency as catalysts for the generation of H_2 under UV irradiation.[33,128–132] The physical dimensions of these NTs control the overall efficiency of water splitting. When the scattering of light within the structures increases, a higher rate of H_2 generation can be expected.[129] Paulose *et al.*[33] fabricated self-aligned TiO_2 NTs (134 μm length, 20–150 nm pore diameter) by anodization using a process in which the pore size and length could be tuned (Fig. 10a–c). After annealing the amorphous NTs at 550 °C, a photoconversion efficiency of about 16.25% was achieved under UV illumination. Mor *et al.*[128] demonstrated Ti–Fe–O NTs based on thin films with an H_2 production rate of about 7.1 mL W^{-1} h^{-1}. Eder *et al.*[133] reported Fe/Pt–TiO_2 NTs with superior electron lifetimes and efficient charge separation under UV light.[131,134] Bulk recombination is reduced by the NT architecture (porosity), while the photogenerated minority carriers (holes) can be trapped by surface states based on a model proposed by Lubberhuizen *et al.*[135] For example, the typical time needed for holes to reach the surface is about 10^{-10} s in nanoporous GaP.

It is known that the noble metals (*e.g.* Au,[136,137] Pt,[46,133,138] Ag[139] and Pd[140]) and many co-catalysts (*e.g.* NiO_x[46]) act as electron reservoirs (acceptors)[138] and collect photogenerated electrons from the CB of semiconductors in close contact. As a result, recombination is delayed, *i.e.* there is Fermi level (E_F) equilibration of the metal and the semiconductor. Delayed recombination helps to enhance the activity of the catalyst. Pt is special because it has a favourable H^+ chemisorption energy and a high activity for proton reduction reactions and it also has a low electrochemical impedance to discharge the absorbents.[138] This is discussed in detail in Tongying *et al.*[126] Pt forms a Schottky junction with TiO_2, which is crucial for the generation of H_2. However, the formation of the Schottky barrier is prevented when Pt is calcined at 873 K.[141] As an additional advantage, these noble metals are not photocorrosive. However, an optimum loading of Pt should be maintained because excessive loadings decrease the production of H_2 as a result of the decreased SA for chemisorption.[142,143] The performance of Au depends on the shape and structure of the NTs.[137]

TiO_2 NTs with Au NPs have shown enhanced H_2 production.[136] Pd quantum dots (QDs) have been used in conjunction with TiO_2 NTs in a solution containing Na_2CO_3 and ethylene glycol (EG) with significant results.[140] Fig. 10a–c shows SEM images of TiO_2 NT arrays with Pd QDs; the evolution of H_2 is shown in Fig. 10d.[140] The measurements were performed at -0.3 V *versus* a standard calomel electrode containing 2 M Na_2CO_3 + 0.5 M EG solution under 320 mW cm^{-2} irradiation for a Pd weight percentage of 2.15. Pt NPs have been used extensively in conjunction with TiO_2 NTs,[144] with a reported QY of about 16% under UV irradiation.

The recombination rate of e–h pairs in TiO_2 NTs is reduced in the presence of Ag NPs (Fig. 11a–c). The yield of H_2 (about 10.69 μmol h^{-1}) is dependent on the anodization voltage

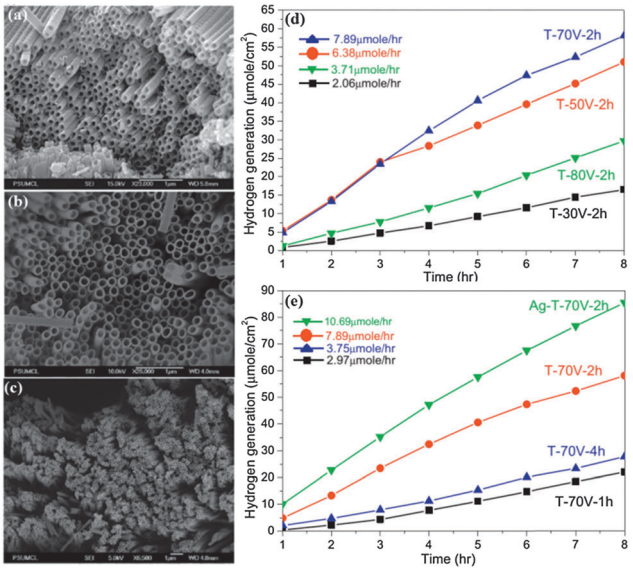

Fig. 11 FE-SEM images of NT arrays produced by anodization at (a) 60 V, 0.25 wt% NH_4F in EG, (b) 40 V in dimethyl sulfoxide with 2% HF, (c) 60 V in DMSO containing 2% HF. H_2 generation measured from (d) TiO_2 NTs produced at different anodization voltages and (e) Ag-modified TiO_2 NTs and unmodified NTs with respect to anodization time. Reproduced with copyright permission from ref. 33 and 139.

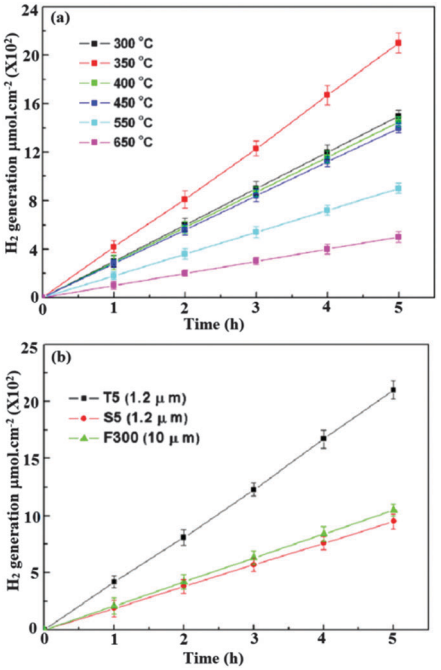

Fig. 12 Amount of H_2 generated from catalysts produced (a) at different annealing temperatures and (b) by highly ordered TiO_2 NTs in the first (F300), second (S5) and third (T5) anodization. Reproduced with the copyright permission from ref. 146.

and time (the texture of TiO_2 NTs)[139] (Fig. 11d and e). A smooth texture provides a better channel for the transport of electrons with minimal scattering. Similar results have been reported by Li *et al.*,[145] who showed that the morphology, anodization potential and time were interlinked with the efficiency of H_2 production.

An annealing temperature of about 350 °C has been found to be optimum for TiO_2 NTs.[146] At higher annealing temperatures, the barrier thickness of the NT arrays and Ti substrate becomes thicker, which inhibits the transfer of charge to the Ti substrate. Fig. 12 shows the generation of H_2 with respect to temperature and cycle times. W-doped (W^{6+} state) TiO_2 NTs were investigated under a glycerol/fluoride electrolyte and the production of H_2 was about 24.97 μmol h^{-1}, depending on the W loading and annealing temperature.[147] The effect of the processing parameters was extended to Ta_2O_5 NTs by Gonçalves *et al.*,[148] who suggested that the anodization potential, electrolyte temperature (diameter, length of NTs) and annealing temperature influence the generation of H_2 with ethanol as an SR. Fig. 13 shows the current densities at different electrolyte temperatures, from which the variation in length and diameter of the tubes can be seen. Gonçalves *et al.*[148] observed that CO, CO_2, CH_4, C_2H_4 and C_2H_6 gases were produced during ethanol photo-reformation. The amount of gas generated increased with increasing annealing temperature.[148] Single crystalline NT arrays of $SrNb_2O_6$ with rhombic cross-sections showed superior H_2 evolution compared with their bulk counterparts as a result of the smaller diffusion length of the charge carriers, in addition to the high SA.[46] This was further enhanced (to 102 μmol g^{-1}) by introducing NiO_x and Pt by impregnation and photodeposition methods, respectively.

H_2 production efficiencies can be enhanced by carbon-rich catalysts such as graphene, multiwalled carbon NTs (MWCNTs),

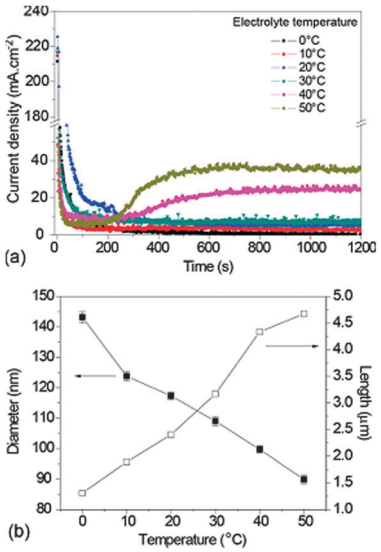

Fig. 13 (a) Current density curves for anodization of Ta discs at 50 V at different electrolyte temperatures and (b) effect of electrolyte temperature on the outer diameter and length of the NTs. Figure is reproduced with copyright permission from ref. 148.

carbon fibres and activated carbon. Cargnello *et al.*[149] enhanced the generation of H_2 from MWCNTs@M/TiO_2 to about 10 mmol h^{-1} g^{-1} in the presence of methanol as a SR, where M = Pt or Pd. It was also suggested that the nanocomposite with Pt was slightly more active than that with Pd. This is a result of the various positive effects from the MWCNTs, Pt and the metal

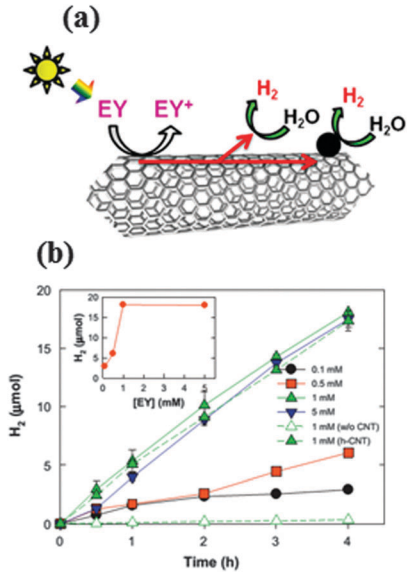

Fig. 14 (a) Schematic illustration of an Eosin Y (EY) sensitized CNT catalyst. (b) H_2 production as a function of EY concentration. This figure is reproduced with copyright permission from ref. 68.

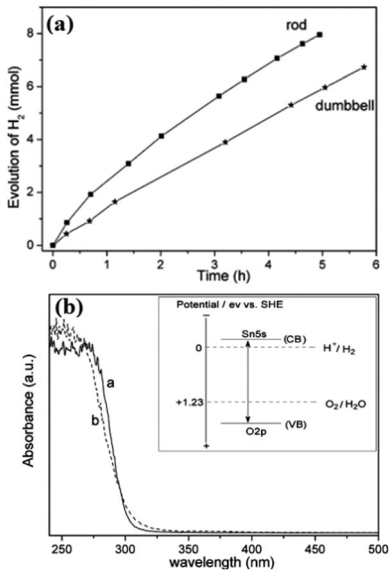

Fig. 15 (a) Evolution of H_2 from $SrSnO_3$ NRs and nano dumb-bells. (b) UV-visible diffuse reflectance spectra of $SrSnO_3$ from NRs (dotted line) and dumb-bell like (solid line) morphologies. Inset shows the band diagram of $SrSnO_3$. Reproduced with copyright permission from ref. 154.

oxide. Primarily, MWCNTs delocalize the photogenerated electrons, thus enhancing the lifetime of the charge carriers, which eventually increases the evolution of H_2.[150]

In a typical investigation,[68] Eosin Y (EY) and triethanolamine (TEOA) were used as a sensitizer and electron donor, respectively, and the MWCNTs showed a nearly nine-fold enhancement in performance compared with other carbon-rich catalysts under simulated sunlight. Fig. 14a is a schematic representation of an EY-loaded MWCNT on which noble metal NPs can also be used. Fig. 14b shows the evolution of H_2 against EY concentration.

4.3. Nanorods

Arrays of NRs have similar effects to NWs, such as a high SA[111,114] promoting surface reactions rather than recombination[151] and short collection lengths for excited carriers in a direction normal to light absorption. Rutile TiO_2 NRs have shown efficient H_2 generation in aqueous solutions containing methanol–water SRs in the presence of Cu^{2+} under UV light irradiation.[152] In addition, the design of a radial p–n junction NR device could provide large improvements in efficiency relative to a conventional planar geometry.[153]

$SrSnO_3$ NR structures were synthesized *via* a hydrothermal method and showed a better H_2 production rate than dumb-bell like structures (Fig. 15a). Fig. 15b shows the UV-visible diffuse reflectance spectra of these NRs and dumb-bells together with a band level diagram for $SrSnO_3$.[154]

Sun *et al.*[155] used Sb-doped SnO_2 NRs as a transparent electrode in the presence of H_2O_2 SR, which improved the conductivity of the scaffold. The improvement in PEC performance is a result of enhanced charge separation efficiency and charge injection efficiency. Controlled incorporation of Sn-doped TiO_2 NRs achieved a good PEC performance.[156] Wang *et al.*[143] reported that the well dispersed CdZnS single crystalline NRs showed higher H_2 generation than CdS when the aqueous solution contained two different SRs (SO_3^{2-} and S^{2-}) with and without Pt under simulated solar light. This enhancement is attributed to the abundant hydrogen reactive sites on CdZnS. However, the incorporation of SRs, co-catalysts, sensitizers, electrolytes and reducing agents yielded a better performance.[144] The parameters affecting the catalytic activity of SRs are not yet well understood. A higher activity is associated with the proton-exchange capability of the materials. Sometimes the native material performs better in the absence of co-catalysts.

Nanostructures of Zn_2GeO_4 have been reported by a number of researchers.[25,76,77,157,158] Liang *et al.*[76] reported on hexagonal Zn_2GeO_4 NFs and NRs (Fig. 16a and b) and compared the evolution of H_2 with its bulk counterpart (Fig. 16c). The results suggest that Zn_2GeO_4 NRs show better H_2 evolution than the NFs and bulk particles where the NRs have predominant reflections from the (110), (21$\bar{0}$), (12$\bar{0}$), (1$\bar{1}\bar{0}$), (2$\bar{1}$0) and (1$\bar{2}$0) planes. Another study on Zn_2GeO_4 suggested that a rhombohedral phase crystal orientation yields better H_2 evolution.[77] Similar to the TiO_2 nanostructures (section 4.2), the process parameters of Zn_2GeO_4 play a crucial part in determining the efficiency of catalytic H_2 generation. Lin *et al.*[157] studied the evolution of H_2 in relation to the calcination temperature of Zn_2GeO_4 NRs. The results (Fig. 17) suggested that a higher calcination temperature (1000 °C) gives a performance as high as 430 μmol h^{-1} g^{-1}, which is nearly seven times higher than that of a sample calcined at 400 °C.[157] However, the SA dropped to one-fifth of that of the sample calcined at 400 °C. Although the SA influences H_2 production, a more crucial parameter is the quality of the crystal and its facets.[25,77] Yan *et al.*[25] reported that Zn_2GeO_4 NRs have the best performance with 3 wt% of RuO_2. The overall water splitting performance depends on the synthesis temperature; NRs obtained at lower temperatures (40 °C) had a dominant

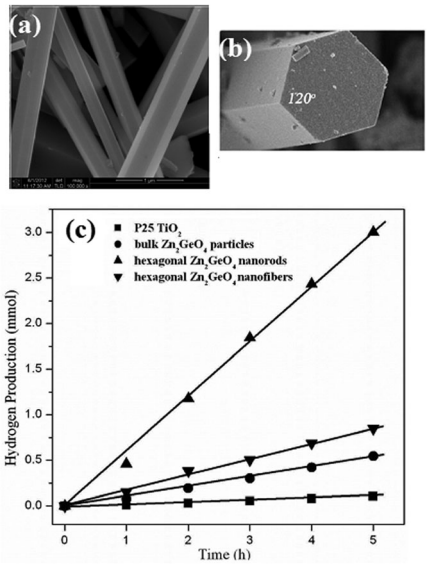

Fig. 16 FE-SEM images of (a) Zn_2GeO_4 NFs and NRs samples obtained at 200 °C with 1.6 g of NaOH, (b) cross-sectional view of an NF and (c) rate of evolution of H_2 from an aqueous MeOH solution compared with various photocatalysts under UV light. Amount of catalyst, 0.1 g; volumes of H_2O and CH_3OH, 55 and 5 mL, respectively. Figures are reproduced with copyright permission from ref. 76.

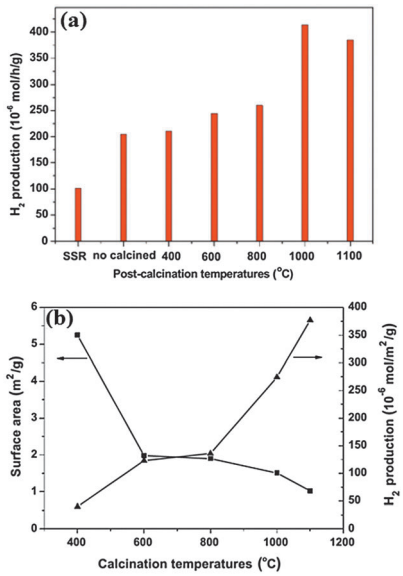

Fig. 17 (a) Evolution of H_2 from Zn_2GeO_4 samples calcined at various temperatures. Conditions: photocatalyst, 0.1 g; Pt co-catalyst, 0.1 wt%; and aqueous MeOH solution (100 mL of 20 vol%). (b) Surface area plotted against calcination temperature showing evolution of H_2. Reproduced with copyright permission from ref. 157.

(110) crystal face. This face may induce strong CO_2 gas adsorption and hence higher H_2 production. Liang *et al.*[158] reported a method for crystal orientation and the self-assembly of Zn_2GeO_4 NRs.

Similar to other core–shell heterojunction catalysts, Yang *et al.*[159] reported the fabrication of In_2O_3–In_2S_3 core–shell NRs that showed a better performance than their individual NR counterparts. Fig. 18 shows the band diagram of the interface of the In_2O_3 and

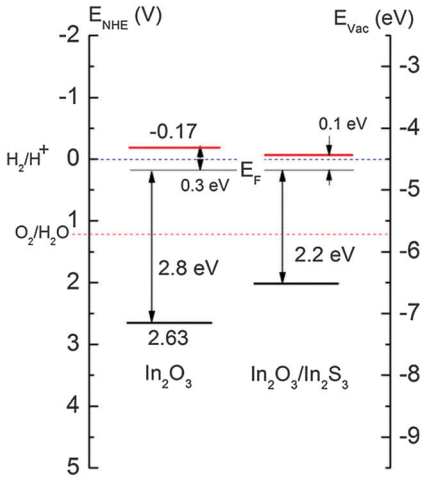

Fig. 18 Band level diagram for In_2O_3 and In_2S_3 core–shell interfaces. Figure redrawn from ref. 159.

In_2S_3 shell, where the energetic alignment of the bands favours the transfer of both electrons and holes to the shell layer (type I band alignment). It is notable that, if the electrons and holes are transferred to the shell region, then the recombination is delayed, yielding O_2 and H_2, which may cause a back-reaction.

4.4. Electrospun nanofibres

Electrospinning is a versatile and convenient technology to produce 1D nanostructures,[160–163] although there are other physical and chemical methods to synthesize fibres.[164–169] 1D NFs are important in electronics, optoelectronics, magnetic sensors,[170] photo-dye degradation,[36,171–173] photocatalysis[174] and in energy-harvesting technologies.[175–178] Functional electrospun NFs have important optical[179–185] and/or electronic properties.[186–197] In the context of H_2 production, TiO_2 electrospun NFs (Fig. 19) perform better than nanostructures produced by hydrothermal synthesis,

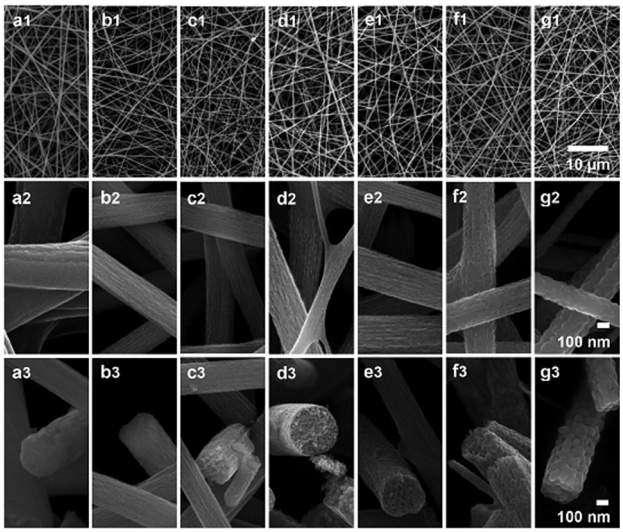

Fig. 19 SEM images of (a) as-spun TiO_2 precursor NFs and NFs after calcination for 3 h at (b) 300 °C, (c) 400 °C, (d) 450 °C, (e) 500 °C, (f) 600 °C and (g) 700 °C. Reproduced with copyright permission from ref. 117.

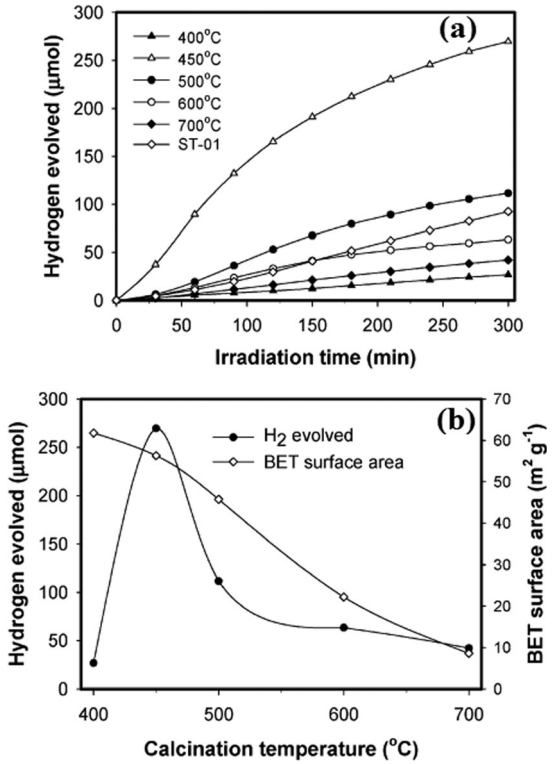

Fig. 20 (a) H_2 production with TiO_2 fibres calcined at various temperatures. (b) Dependence of the calcination temperature on the BET surface area. This figure is reproduced with copyright permission from ref. 117.

where process parameters such as the calcination temperature, crystallinity and SA are determining factors (Fig. 20).[117]

The results suggest that a calcination temperature of 450 °C is the optimum to give the highest yield. However, although calcination at 400 °C gave the highest SA, the H_2 evolution is not significant, as a result of the lowered crystallinity (Fig. 20b). Similar to NRs and NWs, noble metal NPs are used in conjunction with NFs and act as an electron skin, enhancing H_2 production. Zhang *et al.*[118] used Au and Pt NPs simultaneously in the presence of SRs (0.1 M L-ascorbic acid at pH 4.0). Their results suggested that the best combination is $Au_{0.25}/Pt_{0.25}/TiO_2$.[118] Zhang *et al.*[118] reported that no H_2 is evolved for Au NPs under surface plasmon resonance illumination (about 550 nm or visible light). The process of electrospinning can also be applied to mixed oxides such as TiO_2–SnO_2[119] and the calcination temperature plays a key part in the efficiency of H_2 generation (methanol is used as an SR). Another catalyst combination is $SrTiO_3$–TiO_2 NFs, for which the efficiency is better than the individual counterparts when a water–methanol mixture is used as a SR under UV irradiation.[198] Similar to the earlier examples, the H_2 yield is dependent on the calcination temperature and the SA.[120] These composite fibres contrast with core–shell structures where the combination of materials can be selected so that electrons are transferred to the shell region and holes are transferred to the core region. However, in composite structures, the recombination of photogenerated electrons and holes is delayed during the transfer while both stay within the structure. The long NF structure and larger specific SA are advantageous for catalytic activity.[121] Our group has reported the development of MWCNT–TiO_2 NFs and their H_2 generation capability.[44]

4.5. Two-dimensional nanostructures

2D nanostructures such as nanobelts (NBs),[199–201] NSs,[202–204] nanoplates,[205–207] nanolayers,[208,209] nanoribbons,[115,210] and nanoleaves[211] are also efficient for the production of H_2. The transfer of charge carriers to the surface takes place in a similar manner to 1D structures and helps to enhance performance.[201,212–216]

Pure TiO_2 NS surfaces are catalytically inactive as a result of the presence of a large over-potential and fast backward reaction (generation of H_2O), whereas surface-fluorinated Pt–TiO_2 NSs have significant catalytic activity.[217] However, in sharp contrast, ultrathin TiO_2 NSs showed a high catalytic activity as a result of a shorter migration time, which suppressed recombination.[218] Fig. 21a shows the process of producing photogenerated electrons and holes at the TiO_2 surface, where Pt acts as an electron skin (Fig. 21b). However, an optimum amount of Pt should be determined because further increases in the Pt content decrease the production of H_2 (Fig. 21c). TiO_2 NSs showed a better performance than commercial TiO_2 anatase powder,[219] whereas TiO_x NSs fabricated by photodepositing the metal and metal oxide showed enhanced activity[203] with slower e–h recombination in the TiO_x NSs than in the single crystalline counterparts. In single crystalline NSs, the photogenerated electrons react at the edge of the NSs while, in contrast, the holes react over all of the surface.

ZnO NB arrays have shown better activity than thin films or the rod/comb-like ZnO nanostructures under similar conditions.[199] Micro- and nanocomponents of ZnO were combined by Lu

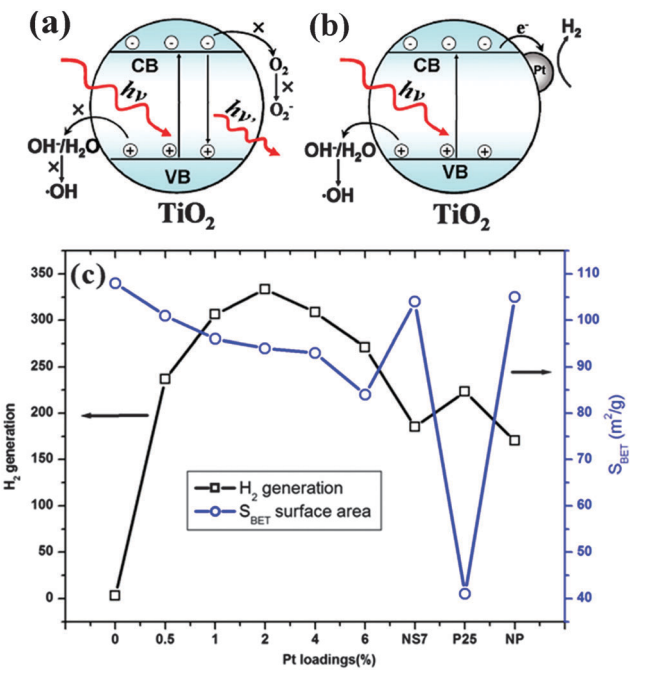

Fig. 21 Probable dynamics of photogenerated electrons and holes on the surface of TiO_2 in (a) a clean anaerobic environment and (b) in the presence of Pt.[217] (c) H_2 generation with respect to the surface area and Pt loadings in TiO_2 (fluorinated). NS7 = without fluorination, P25 = Degussa and NP = NPs of TiO_2. Figure is reproduced with copyright permission from ref. 217.

et al.,[7] in which NS networks on hexagonal pyramid-like microcrystals were studied to determine their catalytic performance. In this complex structure, electrons were transferred from the NSs of high electrical potential to the core micro-pyramids of low electrical potential; this reduces the probability of photogenerated e–h recombination. NiO hollow microspheres showed greater catalytic activity than rods[6] because the microspheres facilitated a higher density of active sites and a better surface charge carrier transfer rate.

Semiconducting niobate NSs were integrated[220,221] into two-component nanostructure systems with separate sites for water reduction and oxidation. Although WO_3 is inactive for H_2 evolution, its derivative $Na_2W_4O_{13}$ is active for overall water splitting from aqueous solutions containing SRs where the later have a layered structure (see ref. 247 cited in Chen *et al.*[222]). Bi_2WO_6 nanoplates were reported by Zhang and Zhu.[206] Kale *et al.*[8] reported that $CdIn_2S_4$ nanostructures with a marigold-like morphology composed of numerous nanosized petals displayed significant H_2 production from H_2S in KOH aqueous solution.

A special class of 2D NSs self-assembled into a 3D architecture is another important research area in photocatalysis.[6–11] Layered titanates have been introduced for H_2 production as a result of their proton-exchange capability in the absence of co-catalysts.[223,224] Sodium trititanate ($Na_2Ti_{3-x}M_xO_7$), potassium tetratitanate ($K_2Ti_{4-x}M_xO_9$) (where M = Mn, Fe, Co, Ni, Cu and x varies from 0.15 to 0.30) and their substituted samples with SiO_2-pillared structures at the interlayer showed high activities.[223] Fig. 22 shows the effect of the BET SA of the unsubstituted tri- and tetratitanates with respect to H_2 generation. Layered double hydroxides have the general formula $[M^{II}_{(1-x)}$–$M^{III}_x(OH)_2]A^{n-}_{x/n}\cdot mH_2O$, where M^{II} is a divalent metal cation (*e.g.* Mg^{2+}, Co^{2+}, Ni^{2+} or Zn^{2+}), M^{III} is a trivalent metal cation (*e.g.* Al^{3+}, Cr^{3+}, Ga^{3+} or Fe^{3+}) and A^- can be an organic and/or inorganic anion (see references cited in Parida *et al.*[209]). These layered hydroxides can be doped with a cation at the octahedral sites, which yields properties similar to doped semiconductors. Mg/Al layered double hydroxides with incorporated Fe^{3+} showed significant H_2 production.[209] Compton *et al.*[220,221] reported calcium niobate ($HCa_2Nb_3O_{10}$) NSs with Pt for photochemical generation of H_2. Ferroelectric materials, such as the stibiotantalites, $SbMO_4$ (M = Nb, Ta) were investigated for H_2 production in the form of NPs.[208] The evolution rate of H_2 from $SbTaO_4$ (3.72 eV) was approximately twice as high as that of $SbNbO_4$ (3.12 eV) and was further enhanced after the incorporation of a RuO_2 co-catalyst. The differences in activity are attributed to the higher CB edge of $SbTaO_4$ (Ta 5d orbitals in TaO_6 octahedral configuration) and the high dielectric constant, which enhances the photogenerated charge separation.

Polyoxometalates, such as $Bi_2W_2O_9$, $BaBi_4Ti_4O_{15}$ and Bi_3TiNbO_9 layered structures, are highlighted for H_2 evolution in the presence of SRs in a review article by Yamase.[225] Scheelite-structured $PbMoO_4$ shows activities for H_2 and O_2 evolution in the presence of SRs under UV irradiation. The substituted compounds $Na_{0.5}Bi_{0.5}MoO_4$, $Ag_{0.5}Bi_{0.5}MoO_4$, $Na_{0.5}Bi_{0.5}WO_4$ and $Ag_{0.5}Bi_{0.5}WO_4$ are also active for O_2 evolution;[222] however, molybdates and tungstates only respond to UV. Pb, Bi and Ag play important parts in the structure of the VB. Solid solutions of b-Ga_2O_3 and In_2O_3 consisting of d^{10} cations have been systematically studied for H_2 or O_2 evolution from aqueous solutions in the presence of SRs. In these catalysts, the band gap and luminescent energy decrease as the ratio of indium increases.[222]

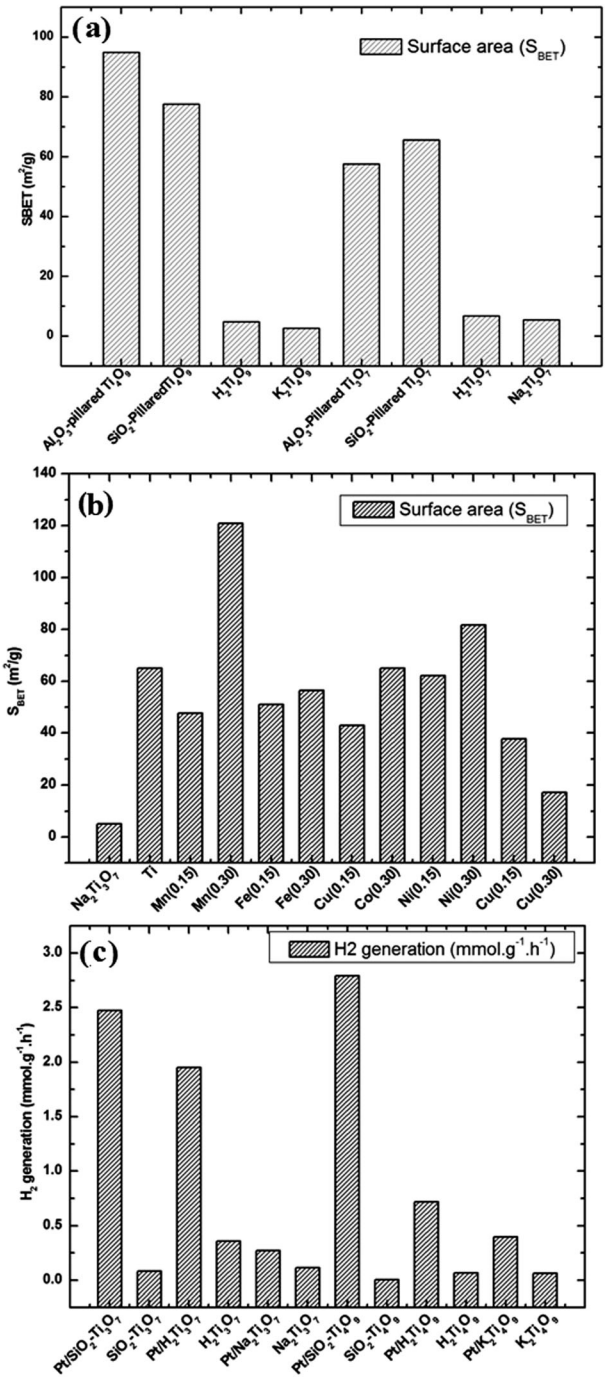

Fig. 22 Properties of different semiconductors: (a, b) BET surface area and (c) H_2 production. The figure is redrawn based on the results from ref. 223.

Sabio *et al.*[226] reported that hydroxide-supported calcium niobium ($HCa_2Nb_3O_{10}$) NSs had a superior H_2 production rate under UV irradiation in the presence of SR or co-catalysts. NSs produced H_2 at a high rate compared with their bulk

Table 2 UV-active nanocatalysts for water splitting

Catalyst	SA (m^2 g^{-1})	E_g (eV)	Co-catalyst/SR	Light source (UV-visible)	Catalytic activity H_2 (μmol h^{-1})	Ref.
Nanowires						
$LiNbO_3$	28		RuO_2	300 W Xe	275	26
$LiNbO_3$	28		RuO_2	400 W Hg	47	26
Si/Cu_2O			Pt/Na_2SO_3–Na_2S	300 W Xe	95	59
$ZnO/Zn_xCd_{1-x}Te$		1.48	Na_2SO_3–Na_2S	300 W Xe	265	35
CdSe/CdS N-doped TiO_2			Pt	520 nm LED	434.29	126
N-doped TiO_2			$Pt/EtOH–H_2O$	3.15 W UVA	700	127
				3.0 W UVB	2250	127
Nanotubes						
TiO_2			Pt/Ag	365 nm, 50 mW cm^{-2}	10.69	139
TiO_2			Pt/EG ($NH_4F–H_2O$)	300 W Xe	420	146
Ti–Fe–O			Pt/KOH	300 W Xe	7.1 mL W^{-1} h^{-1}	128
Titania			Pt	50 W metal hydride	960 μmol h^{-1} W^{-1}	129
$NiO_xSrNb_2O_6$	8.1		Pt	450 W Hg	102	46
TiO_2			$Pt/EtOH–H_2O$	150 W Xe–Hg	0.98	144
TiO_2			Pt/glycol and NH_4F	300 W Xe	0.57 mL h^{-1} cm^2	145
W-TiO_2			Na_2S + Na_2SO_3	300 W Xe	24.97	147
Ta_2O_5	16.2		$EtOH–H_2O$	240 W Hg–Xe	2600	148
TiO_2			NH_4F/EG (ETG)/Au	150 W Hg–Xe	0.65 μmol cm^{-2} h^{-1}	136
CNT	194		Eosin Y (EY)–TEOA	Solar simulator (100 mW cm^{-2})	18	68
Pd/TiO_2			Na_2CO_3 and EG	300 W Xe	592 μmol h^{-1} cm^{-2}	140
Nanorods						
$SrSnO_3$	0.5	4.1	$Pt/AgNO_3$	200 W Hg–Xe	8200	154
$(Cd_{0.8}Zn_{0.2})S$	72	2.4	SO_3^{2-} (Na_2SO_3)	300 W Xe	1710	143
			S^{2-} (Ns_2S)	300 W Xe	3020	143
Zn_2GeO_4			MeOH	125 W Hg	6240	77
	33.2	4.67	Na_2SO_4	125 W Hg	6000	76
			MeOH	150 W Hg	430	157
	36	4.67	$MeOH–H_2O$	300 W Xe	4900	158
	33.1		RuO_2	300W Xe	17.4	25
In_2O_3–In_2S_3			$MeOH–H_2O$	300 W Xe	61.4	159
TiO_2	64.19		$MeOH–H_2O/Cu^{2+}$	400 W Hg	3000	152
Nanofibres						
TiO_2	56.3		MeOH	450 W Hg	54	117
$SrTiO_3$	31.3		MeOH	450 W Hg	167	120
$SrTiO_3/TiO_2$	98.26		$MeOH–H_2O$	400 W Hg	About 1100	198
$Au/Pt/TiO_2$		3.2	L-Ascorbic acid	300 W Xe	11.66	118
$TiO_2/SrTiO_3$	98.26		$MeOH–H_2O$	400 W Hg	1100	121
TiO_2	47.45			400 W Hg (UV)	90	121
TiO_2 (500 °C)	96.3			Visible	206	85
TiO_2 (500 °C)	58.2			450 W Hg	19.1	93
TiO_2/Pt (500 °C)	96.3			>420 nm (visible)	7110	85
TiO_2/CuO (450 °C)	108.1			400 W Hg (UV)	62.7	228
TiO_2/SnO_2 (450 °C)	73.1		$MeOH–H_2O$	400 W Hg (UV)	200	119
TiO_2/MWCNT	600		Pt/parylene	150 W Xe	691	44
Nanolayers						
$SbNbO_4$	1.66	4.1	RuO_2	450 W Hg	24	208
$SbTaO_4$	1.53	3.9	RuO_2	450 W Hg	58	208
Fe^{3+}–Mg/Al	62		MeOH	125 W Hg	301	209
Nanoribbons						
CdSe			Na_2SO_3–Na_2S	175 W Hg	106.79	115
Nanoleaves						
$Na_2Ti_4O_9$		4.11	$MeOH–H_2O$	350 W Hg	5.72	211
Nanosheets						
Pt/TiO_2	94		EtOH	350 W Xe	333.5	217
Nanosheets						
$HCa_2Nb_3O_{10}$		3.53	Pt	175 W Hg	78.37 μmol	220
$HCa_2Nb_3O_{10}$		3.53	Pt	175 W Hg	49.15	221
Tetrabutyl ammonium–$Ca_2Nb_3O_{10}$			$Pt/MeOH–AgNO_3$	350 W Xe	3231.40	226

Table 2 (*continued*)

Catalyst	SA (m^2 g^{-1})	E_g (eV)	Co-catalyst/SR	Light source (UV-visible)	Catalytic activity H_2 (μmol h^{-1})	Ref.
TiO_2			MeOH–H_2O	150 W Xe	6000	227
Flower TiO_2 (500 °C) anatase	31.7		MeOH–H_2O	450 W Hg	117.6	219
Flower TiO_2 (500 °C)	31.7			450 W Hg	588	
Photonic crystals						
TiO_2	75.5		CH_3OH	500 W Xe lamp	247 μmol h^{-1}	41
N-TiO_2 leaf	103.31		Pt/methanol	400 mW cm^{-2} Xe lamp	1401.70 μmol h^{-1}	81

counterparts. The structural conversion of TiO_2 NPs to NSs showed their high catalytic activity for H_2 generation and the removal of environmental pollution.[227] Pt-loaded TiO_2 hierarchical photonic crystals[41] have shown a doubling of efficiency. The rate of hydrogen production was 247 μmol h^{-1} and the QY was about 11.9%. The experimental results showed that the stop band reflectivity was suppressed, enhancing the evolution of H_2. Zhou *et al.*[81] fabricated a leaf-like structure by copying the complex architecture of leaves and replacing the natural photosynthetic pigments with catalysts to realize an efficient catalyst. The use of 20% aqueous methanol as an SR might have improved the rate of evolution of H_2 (Table 2).

5. Modified visible light active photocatalysts for hydrogen generation

Photogenerated electrons easily recombine with holes in semiconductors. This recombination leads to the low quantum efficiency (QE) of photocatalysis. SRs can effectively restrain this recombination process and improve the QE. Several common approaches have been adopted to activate wide band gap materials to visible light for water splitting: (1) doping with metal and/or non-metal ions; (2) controlling the band structure by developing solid solutions; (3) dye sensitization; (4) band gap engineering; and (5) combining wide band gap materials with visible light active semiconductors. The visible light activity of nanostructured materials has been important in enhancing the efficiency of electron injection to the CB in photocatalysts.

5.1. Nanowires

The fabrication and doping of a variety of nanostructures has improved the activity of PEC water splitting. The confined dimensionality of 1D and 2D structures offers enhanced light absorption as a result of the large active SA and ultrafast charge transport behaviour. In the introduction, we outlined the thermodynamic requirement[24] that must be met to avoid catalyst corrosion. However, CdS (E_g = 2.4 eV) is very effective in splitting water under visible light irradiation[229] in the presence of SRs such as S^{2-} and SO_3^{2-}. Fig. 23 shows the effect of SA and generation of H_2 with respect to synthesis temperature. As the synthesis temperature increases, the evolution of H_2 also increases, despite the decrease in the SA (Fig. 23a). The rate of H_2 production was improved by incorporating graphitic (g-C_3N_4) structures with CdS under visible light irradiation (see Table 3).[230] In the presence of Pt and SRs, CdS showed further improvement in H_2 production.[104] Titanic acid NWs/EY in the presence of Pt NPs and TEOA have been shown to yield significant H_2.[231] The performance of NWs was significantly improved by introducing Au NPs;[137] it was noted that the H_2 yield depends on the shape and structure of Au. Kibria *et al.*[232] reported GaN NW photocatalysts for spontaneous water splitting to produce H_2 under visible and IR light irradiation.

With respect to heterostructures, CdS–TiO_2 NTs were investigated for H_2 production[233] and the results suggested a QE of about 43.4% under visible light irradiation ($\geq$ 420 nm). The high activity is a result of the quantum size effect and the potential gradient at the interface.[234] Liu *et al.*[234] combined Si (cathode) and TiO_2 (anode) NWs; both the difference in the band gap of

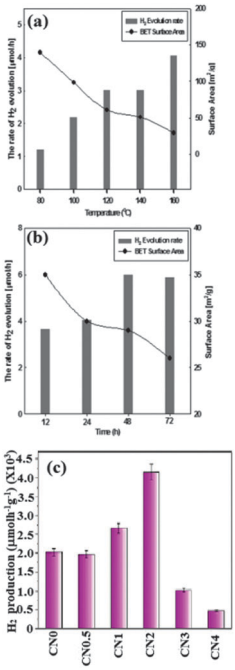

Fig. 23 (a) Rate of H_2 evolution and surface area of CdS samples synthesized by a solvothermal reaction at different temperatures. (b) Synthesis at 160 °C for 12 h, 24 h, 48 h and 72 h. Catalysis: 0.1 g CdS with 1 wt% Pt; 0.1 M Na_2S + 0.02 M Na_2SO_3; 500 W Hg lamp with a cutoff filter ($\lambda \geq$ 420 nm). Reproduced with copyright permission from ref. 229. (c) H_2 production from CdS NWs (CN0) and g-C_3N_4-coated CdS NWs (CN0.5, CN1, CN2, CN3 and CN4) from 0.35 M Na_2S + 0.25 M Na_2SO_3 aqueous solution. Reproduced with copyright permission from ref. 230.

Table 3 Visible light active and/or modified nanocatalysts for water splitting

Catalyst	SA	E_g	Co-catalyst/SR	Light source	H_2 (μmol h^{-1})	Ref.
Nanowires						
CdS	29		Na_2S–Na_2SO_3	500 W Hg	4	229
CdS/g-C_3N_4	22.9		Na_2S–Na_2SO_3	350 W Xe	4152	230
C_3N_4			Pt			270
CdS	73.6	2.43	Na_2S–Na_2SO_3	300 W Xe	260	104
Titanic acid			Eosin Y-sensitized Pt/TEOA	300 W halogen	88.1	231
Rh/Cr_2O_3:p-GaN:Mg		3.4	MeOH	300 W Xe	4000	232
Si-TiO_2			H_2SO_4	150 mW cm^{-2} (1.5 Sun)	875	234
Rh/Cr_2O_3 on InGaN/GaN			Pt	300 W Xe	683	235
InGaN/GaN				300 W Xe		237
Nanotubes						
$Na_2Ti_2O_4(OH)_2$	400		EY/Pt/TEA	300 W halogen	75.45	244
MWCNT			EY/MWCNT/Pt/TEOA	300 W halogen	3.06 mM	245
CdS/TiO_2/Pt/CNTs				100 mW cm^{-2}	70	246
CdS/TiO_2		2.36		350 W Xe	30.3	243
TiO_2	NT		Na_2CO_3–EG	300 W Xe	592	140
CuO/trititanate	87		EtOH	300 W Xe	98	247
Nanorods						
$ZnFe_2O_4$	51		Pt/MeOH	250 W Xe	237.87	251
CuO/trititanate	70			150 W halogen	139.03	248
α-Fe_2O_3	61		NaOH	300 W Xe	60 mL h^{-1}	250
(γ-Fe_2O_3)–(α-Fe_2O_3)	66		NaOH	300 W Xe	75 mL h^{-1}	250
$Ni(OH)_2$/CdS	90		Pt/triethanolamine	300 W Xe	5084	249
Graphitic carbon nitride	52		Pt/triethanolamine	LED lamp	About 28 μmol h^{-1}	272
Graphitic carbon nitride	230		Triethanolamine	500 W Xe	2.45%	273
Nanofibres						
Au/Pt/TiO_2			L-Ascorbic acid	300 W Xe	0.108	254
Cu/TiO_2						274
NiO–TiO_2–carbon						255
CdS–ZnO		2.34	Na_2S–Na_2SO_3	500W Xe	About 354	83
TiO_2/N_2 (450 °C)	70			150-W Xe	28	45
Nanolayers						
Zn–In–S	44.2		Pt	400 W Hg	211.2	267
MoS_2						266
Nanoribbons						
CdSe–MoS_2			Na_2S–Na_2SO_3	300 W Xe	45	269
Nanosheets						
$ZnIn_2S_4$	165.4	2.43	Cetylpyridinium bromide/ Na_2S/Na_2SO_3	250 W Hg	1544.8	268
$ZnIn_2S_4$	103	2.3	Na_2S/Na_2SO_3	300 W Xe >420 nm	57	260
			Pt/Na_2S/Na_2SO_3		257	
CdS/graphene	48		Pt/lactic acid	350 W Xe	1.12 mL	265
CuS/ZnS	37.5		Na_2S–Na_2SO_3	350 W Xe	4147	88
CdS	112.8		Pt/Na_2SO_3	300 W Xe	4.1 mM h^{-1}	259
Flowers						
NiO–CdS	44		Na_2S–Na_2SO_3	500 W halogen	149	264
Metal-free						
mpg-$C_3N_{4/0.2}$	69		Pt/triethanolamine	500W Hg	149	271
g-C_3N_4	10		MeOH–H_2O	>420 nm	10.7	272
Microspheres						
$ZnIn_2S_4$ (prepared with 0.21 g CPBr)	165.4	2.43	Na_2S–Na_2SO_3	250 W Hg	766.8	268
$ZnIn_2S_4$ (prepared at pH 2)		2.34			1544.8	

these materials and the band alignment are notable (Fig. 24). In this instance e–h pairs are generated in Si and TiO_2 under illumination during the absorption of different wavelength regions of the solar spectrum. The band bending shown in Fig. 24d favours the transfer of electrons from TiO_2 to recombine with holes in Si. The electrons from Si and holes from TiO_2 take part in H_2 and O_2 generation, respectively.

1D NWs of the multi-band gap metal nitride (InGaN–GaN) heterostructure facilitated efficient matching and use of the incident solar irradiation.[235] InGaN–GaN NWs with various doping levels of In facilitated a broad range of absorption wavelengths with

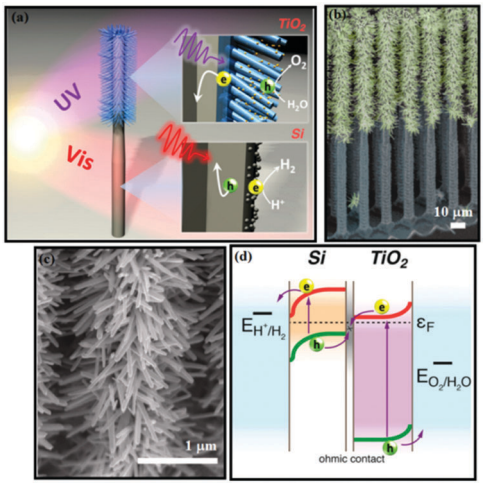

Fig. 24 (a) Schematic diagram of Si/TiO_2 tree-like heterostructures. (b) False-colour SEM image of an Si/TiO_2 nanotree. (c) Magnified SEM image and (d) band gap diagram of the two components. This figure is reproduced with copyright permission from ref. 234.

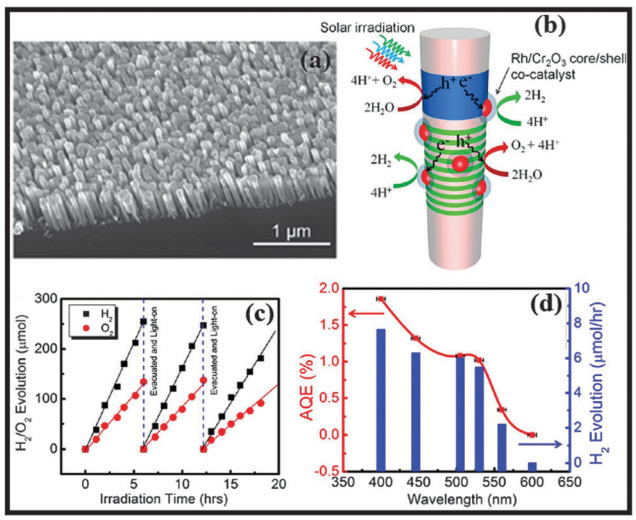

Fig. 25 (a) SEM image of GaN/InGaN NW grown on an Si substrate. (b) Water splitting mechanism on Rh/Cr_2O_3/InGaN/GaN catalyst. (c) Irradiation time *versus* H_2/O_2 evolution. (d) Apparent quantum efficiency (AQE) and H_2 evolution rate against incident wavelength (the FWHM of the optical filters is given as error bars). The H_2 evolution rate was derived from about 2 h of overall water splitting under each optical filter. Reproduced with copyright permission from ref. 235.

co-catalyst Rh–Cr_2O_3 core–shell NPs.[236] Fig. 25a shows the SEM image of GaN–InGaN NWs grown on GaN nanowire templates on an Si(111) substrate; Fig. 25b suggests the reaction mechanism on the co-catalyst and InGaN–GaN NWs. Water splitting takes place on both GaN and InGaN NWs (Fig. 25c) under suitable illumination. With increasing wavelength, the apparent QE decreases (Fig. 25d). Similar work with GaN and InGaN heterostructures have been reported by the same research group.[237]

5.2. Nanotubes

In general, surface defects such as oxygen vacancies on the semiconductors play a crucial part in catalysis.[36,172,173,238–241] The oxygen vacancies serve as adsorption sites depending on their physical location within the catalyst, as well as help to delay recombination.[36,72,173] For TiO_2 NTs, Kang *et al.*[242] suggested that $NaBH_4$ treatment could control the defects on the surface. The treated surface had better electron transfer properties at the semiconductor/electrolyte interface than the parent surface. However, predominant oxygen vacancies will not help to enhance the H_2 production. Similar results were obtained on surface-fluorinated TiO_2 nanoporous films. TiO_2 NTs with Pd QDs as a co-catalyst facilitated a relatively higher efficiency of photocatalytic H_2 generation[140] (Fig. 26).

1D nanostructured titanate NTs are known for their cation-exchange capacities, which allow high loading of the active catalysts. Li and Lu[244] investigated $Na_2Ti_2O_4(OH)_2$ NTs in the presence of triethanolamine (TEA) and Pt. Titanates have been investigated for their photocatalytic degradation of dye molecules,[171] but they should also be considered for H_2 production because of their predominant surface defect densities, which enhance catalysis.

Li *et al.*[245] reported that EY–MWCNTs in the presence of TEOA (electron donor) showed significant H_2 generation under visible light illumination ($\lambda \geq 420$ nm). The role of MWCNTs is similar to that of the noble metals in the context of delaying recombination by trapping electrons and they may be a good substitute for Pt. Type I and type II band alignments consist of two semiconductors such as CdS–TiO_2,[243] whereas ternary (CdS–TiO_2–Pt and CdS–TiO_2–CNTs) and quaternary (CdS–TiO_2–Pt–CNTs) composites have also demonstrated significant H_2 generation. In all these instances, cascaded charge transfer takes place between the TiO_2 and CdS, while the Pt and/or CNTs act as electron collectors.[246] TiO_2 in the form of NTs modified by CdS nanostructures have been investigated[243] (Fig. 27a). p-type Cu–Ti–O

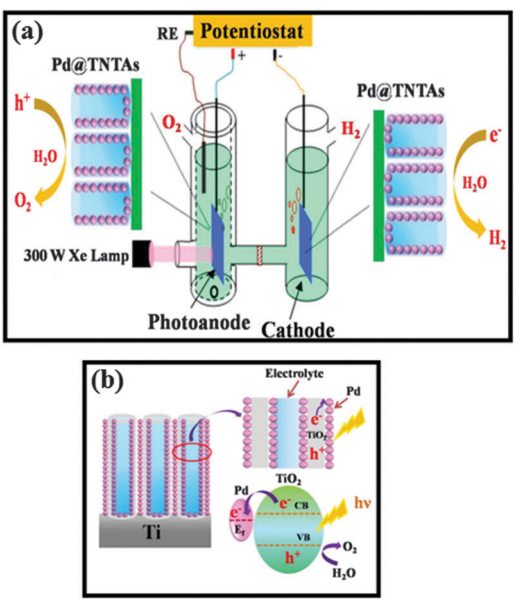

Fig. 26 (a) Schematic diagram of a PEC cell with Pd–TiO_2 NTs and Pt–TiO_2 NTs. Close-up shows both the photoanode and cathode. (b) Schematic diagram of Pd QDs–TiO_2 NTs and the charge transfer process from TiO_2 to Pd (lower right panel). This figure is reproduced with copyright permission from ref. 140.

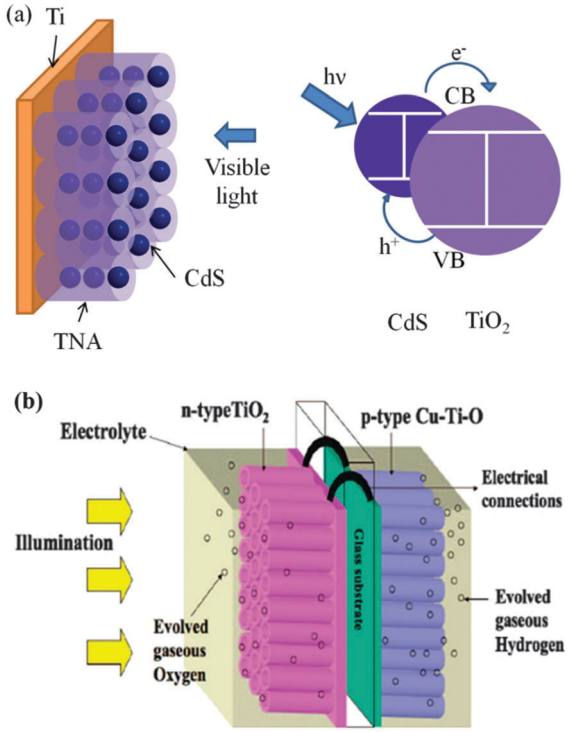

Fig. 27 (a) Schematic diagram of CdS–TiO_2 NTs (left) and the charge transfer process (right). This figures is redrawn based on the results from ref. 243. (b) PEC diode consisting of TiO_2 and Cu–Ti–O NT arrays. The oxygen-evolving TiO_2 side absorbs UV irradiation and the Cu–Ti–O side absorbs the visible part of the spectrum, evolving H_2. Figure is reproduced with copyright permission from ref. 132.

NTs with n type TiO_2 NTs have shown significant photocurrent generation, although they are self-biased as a result of suitable band alignment (Fig. 27b).[132] CdS–trititanate NTs have been investigated for their H_2 generation capability. Effective charge separation is evidenced in this composite, which favours the catalytic activity.[247]

5.3. Nanorods

The incorporation of a small amount (about 1%) of copper ions into TiO_2 NRs gave an improved performance over their pure counterparts under solar light.[248] Doping caused the band gap to shrink from 3.10 to 2.84 eV. However, a further decrease in E_g (2.40 eV at about 3% Cu doping) decreased the production of H_2 by about five times in pure water. In the presence of MeOH aqueous solution, the production of H_2 from 1 and 3% Cu-doped TiO_2 is comparable. It was suggested that a lower band gap may not enhance photon harvest in all instances. Severe doping may cause lattice defects or the formation of a secondary phase that might act as an electron trap, thereby decreasing the production of H_2. However, if the density of the hole traps can be increased, then the H_2 productivity can be increased, or, at least, the back-reactions can be minimized. The morphology and crystal quality help to enhance the generation of H_2, as seen with CdS NRs and nanograins, where NRs gave better results.[113] CdS NRs modified with $Ni(OH)_2$ (23 mol%) showed the highest reported generation of H_2 under visible light

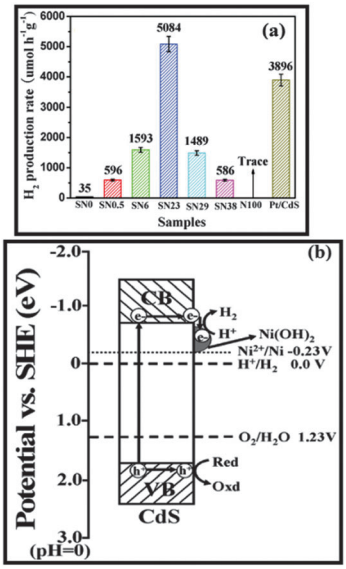

Fig. 28 (a) Comparison of H_2 production for various ratios of CdS to $Ni(OH)_2$ (SN). The ratios (in parentheses) for various samples were SN0 (0), SN (0.5), SN (6), SN (23), SN (29), SN(38), N (100) with 1 wt% Pt–CdS under visible light in a TEA aqueous solution. (b) Proposed mechanism for H_2 production. This figure is reproduced with copyright permission from ref. 249.

irradiation[249] (Fig. 28a). Fig. 28b shows that the potential of Ni^{2+}/Ni is lower than the CB of CdS and more negative than the H^+/H_2 potential. This alignment favours the transfer of electron from the CB of CdS to $Ni(OH)_2$ and the reduction of H^+ to H_2. Based on the band gap of iron oxide (corresponding to absorption in the visible range), maghemite (γ-Fe_2O_3)–haematite (α-Fe_2O_3) core–shell NRs were produced and showed a higher evolution of H_2 from H_2S than their individual NRs.[250] Porous $ZnFe_2O_4$ NRs showed effective evolution of H_2 from an aqueous methanol solution under visible light; the shapes and intra-particle porous structure were beneficial for the rapid transfer of photogenerated carriers onto the surface.[252] The evolution of O_2 was not detected, as a result of the mismatched energy levels of the VB (of $ZnFe_2O_4$) and the oxidation potential of water. Surprisingly, without using any SRs, an Au NRs/TiO_2 cap/Pt NP configuration[252] produced about 2.8 mmol h^{-1} g of H_2. The improved evolution of H_2 was a result of the promotion of trap-bound electrons in the TiO_2 to the CB. These electrons were then captured by Pt to participate in the H_2 evolution.[150]

5.4. Electrospun nanofibres

Metal oxide composite NFs[228,253] have also proved to be efficient in H_2 generation. Zhang *et al.*[254] reported plasmon enhancement of photocatalytic H_2 generation over Au–Pt–TiO_2 electrospun NFs. Yousef *et al.*[255] suggested that the incorporation of transition metal NPs strongly modifies the physiochemical characteristics of the metal oxide nanostructures. Lee *et al.*[254] have shown that TiO_2–CuO composite NFs are promising for H_2 production. Fig. 29a–c shows typical SEM images of the electrospun fibres and H_2 production over time. Charge generation and subsequent catalysis are shown in Fig. 29d. Similar work by the

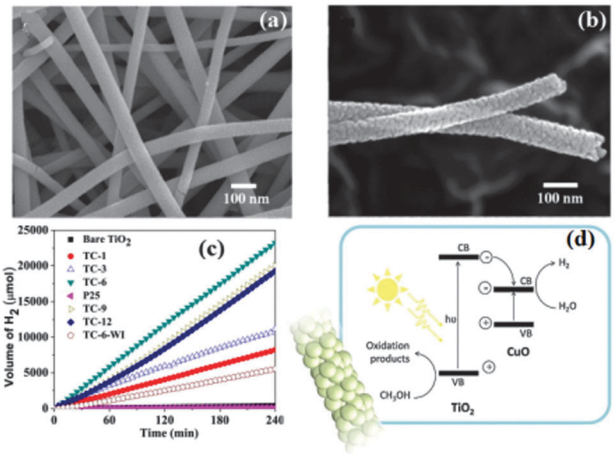

Fig. 29 (a) FE-SEM images of TiO_2–CuO at 6 mol% in Cu NFs. (b) High magnification FE-SEM image. (c) H_2 evolution with time. (d) Schematic band gap diagram of TiO_2/CuO heterojunction. Reproduced with copyright permission from ref. 253.

same research group has also been published elsewhere.[228] It has been reported that the combination of Fe_2O_3 NPs and TiO_2 NFs has advantages over the individual materials and enhances light absorption.[256] An effective strategy to overcome photocorrosion and toxicity problems from CdS-based materials is their incorporation in polymeric NFs. CdS and CdS–PdS NPs were mixed in poly(vinyl acetate) electrospun NFs and the composite produced more H_2 than bare CdS NPs.[257] The efficiency of H_2 generation also depends on the morphology of the NFs.[83] Yang *et al.*[83] reported that electrospun core–shell CdS–ZnO NFs showed excellent H_2 generation under visible light. The activity was mainly attributed to high visible light absorption and low charge carrier recombination. N-doped TiO_2 electrospun NFs were also explored for efficient H_2 generation and the efficiency was found to be dependent on the concentration of the N precursor.[45] Caterpillar-like ZnO nanostructures on ZnO force-spun NFs showed about 0.165% photon-to-hydrogen conversion efficiency;[258] the increase is accounted for by enhanced light-harvesting ability and the effective electron–hole separation.

5.5. Two-dimensional nanostructures

5.5.1. Nanosheets. CdS NSs produced by a two-step synthesis were able to produce H_2 at about 4.1 mM h^{-1} under visible light[259] (Fig. 30a). From earlier results, it is clear that Pt is an excellent co-catalyst. However, it is vital to quantify its loading percentage. As expected, excessive loadings may not increase the yield and the optimum loading is shown in Fig. 30b. This study also optimized the concentration of SRs and H_2 evolution from various cycles (Fig. 30c and d). ZnS (E_g = 3.4 eV) is not active in the visible region, in contrast with $ZnIn_2S_4$,[260] which has an almost five times higher activity in the presence of Pt in the visible region than its pristine counterpart. ZnS NSs have been studied in combination with CuS–Cu_2S in the presence of Na_2S and Na_2SO_3.[88] Fig. 31a shows H_2 production rates from different catalyst combinations. Pristine ZnS (CZ0) has a negligible production of H_2 as its band gap is too large to absorb visible light.

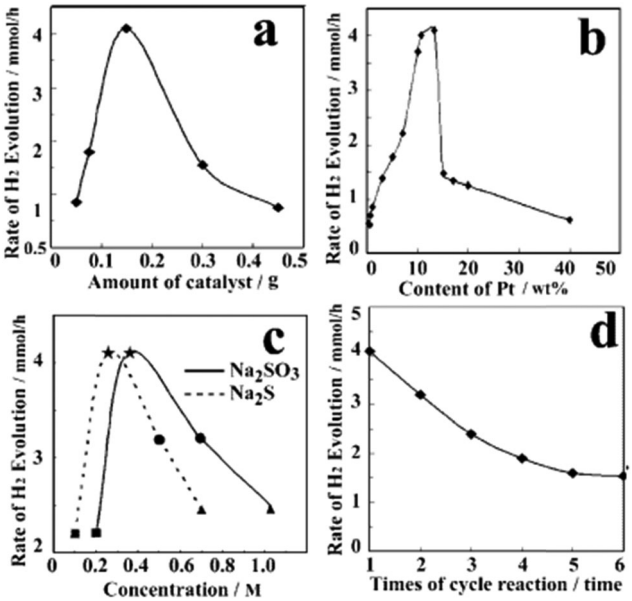

Fig. 30 Evolution of H_2 with (a) amount of CdS catalyst with 10 wt% Pt and (b) Pt loading (0.15 g CdS). (c) Concentration of SRs against H_2 evolution rate from 0.15 g of Pt–CdS and (d) 0.15 g of 10 wt% Pt–CdS. (a), (b) and (d) used a 0.25 M Na_2SO_3 + 0.35 M Na_2S electrolyte. All reactions were performed under visible light. Reproduced with the copyright permission from ref. 259.

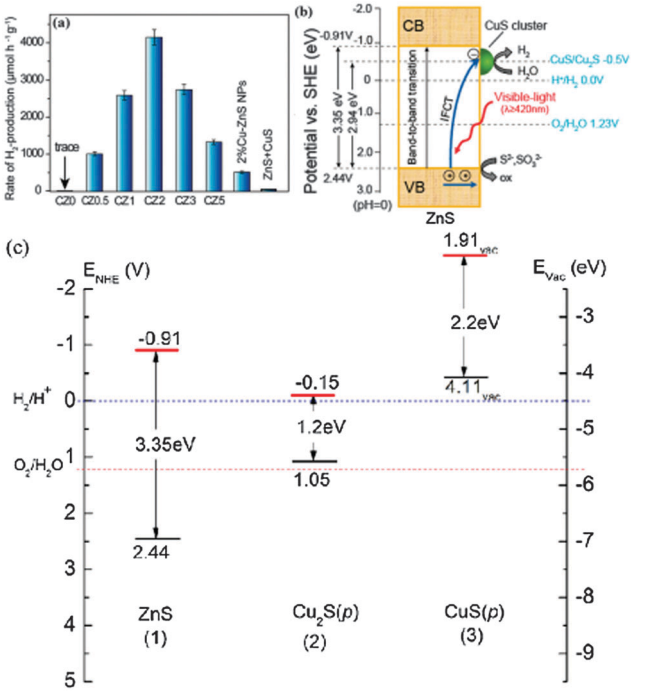

Fig. 31 (a) Comparison of H_2 production using CuS/ZnS porous NSs and ZnS samples under visible light in the presence of 0.35 M Na_2S + 0.25 M Na_2SO_3. (b) Schematic diagram of interfacial charge transfer from the VB of ZnS to the CuS clusters both (a) and (b) are reproduced with copyright permission from ref. 88. CZ0-ZnS, CuS molar concentration denoted as numerals. (c) Energetic values of the CB and VB positions of ZnS, Cu_2S and CuS taken from the corresponding references as follows: ZnS (1),[88] Cu_2S (2)[262,263] and CuS (p) (3). The figure (c) is redrawn based on the results from ref. 88, 261–263.

In contrast, after the addition of small amounts of CuS to ZnS, the generation of H_2 is abruptly increased under visible light irradiation. Fig. 31b shows the mechanism for the production of H_2 by CuS–ZnS porous NSs.

The band-to-band transition of ZnS cannot take place under visible light irradiation due to the large band gap energy. Pure CuS also shows no visible light activity, although the combination CuS–ZnS provides a platform for visible light activity. Zhang *et al.*[88] did not mention the VB of CuS–Cu_2S, but the band diagram suggests a band gap of 2.94 eV where the VBs of ZnS and CuS–Cu_2S are at the same energy level. If we consider the published band diagram of CuS and Cu_2S, the VB of ZnS and CuS or Cu_2S are not energetically in line with each other (Fig. 31c). If interfacial charge transfer has to take place, then the energy difference from the VB of ZnS to the VB of Cu_2S–CuS should be taken into account. In the band gap range 1.2–2.15 eV (CuS–Cu_2S combined), illumination at 420 nm is sufficient to create e–h pairs in these semiconductors. In this instance, the transfer of charge takes place from CuS–Cu_2S to ZnS. The interfacial regions are generally defective and we can therefore expect charge carrier traps within the interface. Another combination of heterostructures is NiO–CdS,[264] where the CdS absorbs visible light and photogenerated electrons are transferred to the NiO. This combination has shown significant H_2 production (Fig. 32a). Fig. 32b shows the band alignment and corresponding charge transfer phenomenon under visible light irradiation.

Graphene, apart from having outstanding electrical conductivity, can also inhibit the recombination of the electron–hole pairs by collecting the electrons and enhancing the absorption of visible light. This phenomenon is similar to that of the noble metal NPs.[265] Fig. 33 shows the mechanism and influence of graphene oxide with CdS clusters for the high efficiency photocatalytic production of H_2 driven by visible light.[265]

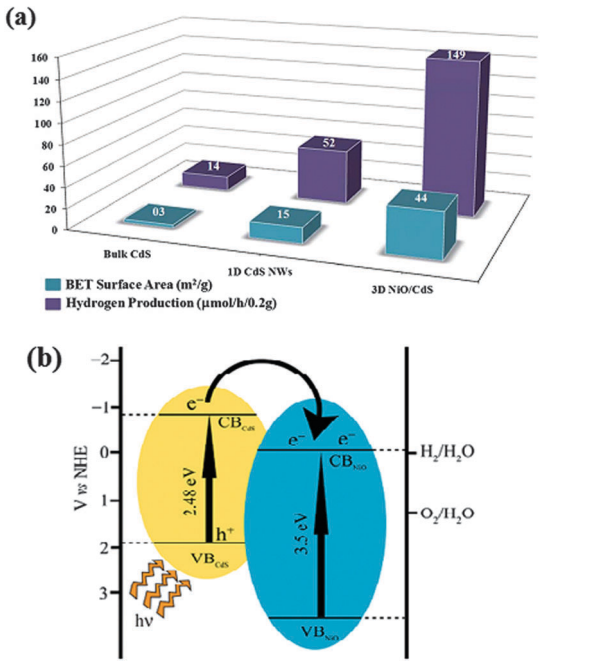

Fig. 32 (a) Surface area and the amount of H_2 generated from bulk CdS, 1D CdS NWs and 3D NiO–CdS photocatalysts under visible light irradiation. (b) Schematic diagram of electron transfer and band diagram for NiO and CdS. Reproduced with copyright permission from ref. 264.

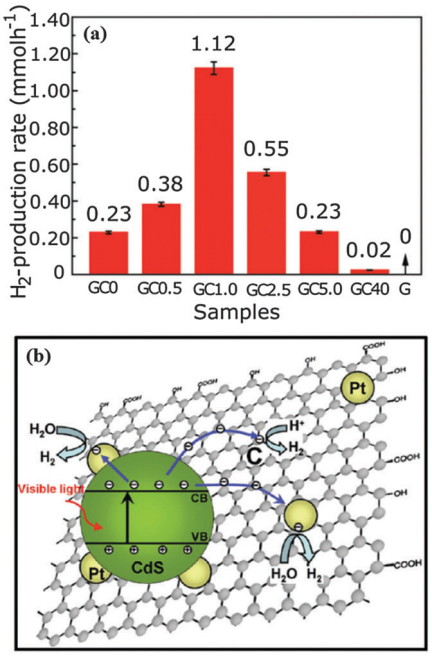

Fig. 33 (a) H_2 productivity of graphene oxide–CdS composites in the presence of 10 vol% aqueous solution of lactic acid and 0.5 wt% Pt. (b) charge generation and subsequent separation under visible light. Reproduced with copyright permission from ref. 265. The weight ratios of GO to $Cd(Ac)_2$ $2H_2O$ were: 0, 0.5, 1.0, 2.5, 5.0 and 40% and the obtained samples are labelled as GC0, GC0.5, GC1.0, GC2.5, GC5.0 and GC40, respectively.

5.5.2. Nanolayers. Simulation studies[266] on MoS_2 layered structures suggest that pristine single-layer MoS_2 is a good candidate for H_2 production. The catalytic activity can be improved by applying a small in-plane compressive strain or an out-of-plane tensile strain. p-type doping (with phosphorus) can also be used to enhance the overall splitting of water. Fig. 34 shows the changes that occur as a result of doping. A layered Zn–In–S photocatalyst in the presence of NaCl also shows high visible light activity for the evolution of H_2.[267] Morphologically similar structures have been produced with $ZnIn_2S_4$ and their activity for H_2 production tested.[268]

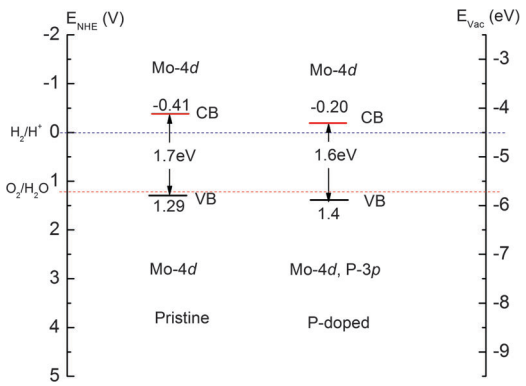

Fig. 34 Band diagram of single-layer MoS_2 and its P-doped counterpart. Figure redrawn based on the results from ref. 266.

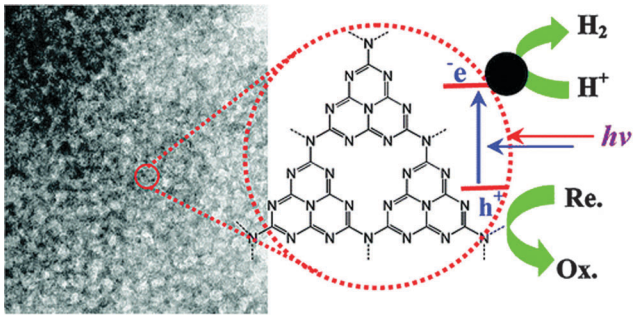

Fig. 35 TEM image of g-C_3N_4 and H_2 evolution under visible light illumination. Figure reproduced with copyright permission from ref. 271.

5.5.3. Nanoribbons. The MoS_2 layered structure has been shown to have potential for the evolution of H_2. In this instance, the MoS_2 layers are exfoliated *via* ultrasonication and chemically linked to CdSe nanoribbons. The resultant composite has a QY of 9.2% at 440 nm, whereas bulk CdSe is not active for this reaction. The overall increase is nearly four times, although this depends on the mass percentage of MoS_2. The chemical linkage of Pt NPs to the CdSe nanoribbons did not influence the evolution of H_2.[269]

5.5.4. Metal-free photocatalysts. Graphitic carbon nitride (g-C_3N_4) has potential for the production of H_2 from water under visible light illumination.[270] Under suitable illumination, the creation of e–h pairs is similar to that in metal oxide photocatalysts, where the electrons are excited to the CB and holes are created in the VB. In this example, the oxidation of H_2O takes place at the N atoms, whereas the C atoms provide reduction sites for H_2 (Fig. 35). A similar study has been reported by Wang *et al.*[270]

The 1D graphitic carbon nitride NRs were synthesized on a template and decorated with Pt NPs.[272] This hybrid material showed a surprisingly high H_2 yield with a low specific SA in the presence of a triethanolamine scavenger. The enhancement is ascribed to the efficient charge separation of the 2D layered structures. Huang *et al.*[273] reported bio-inspired carbon nitride mesoporous NSs composed of nanospheres and with the possibility of H_2 generation.

6. Conclusions and future prospects

Nanomaterials have attracted much attraction and there have been high expectations of innovations in many research areas, including medicine, communications, materials development and energy and environmental technology. At the same time there is growing concern that nanomaterials may be hazardous to both health and the environment. In the energy sector, nanomaterials have great potential as they can be used in energy-absorbing materials, such as batteries, fuel cells and solar cells, for the storage of energy. Although nanomaterials are seen by some workers as the way to meet future requirements, they have some disadvantages. As these particles are very small, problems can arise from their inhalation. Nanotechnology is currently very expensive and further development will be costly; manufacturing difficulties may increase the cost of the products. Realistic market costs of nanomaterials have been reported online.[275]

Environmentally friendly and cost-effective fuels are in great demand and this is why H_2 production is of interest. Although it is a promising technology, there are many challenges that require further development before it can be used on an industrial scale. One challenge is the fabrication of a catalyst that harvests H_2 from a non-conventional energy resource such as solar energy with significant efficiency. Wide band gap semiconductors cannot use the visible region of the solar spectrum. Some small band gap materials require SRs or are unstable in long-term usage because of the thermodynamic requirement of the positions of the CB and VB. SRs can inhibit back-reactions by capturing photogenerated holes,[93] but tend to form CO_2 instead of O_2,[124] which has an adverse effect on the environment. Industrial waste (sulfides from aqueous solutions containing S^{2-} and SO_3^{2-}) can be used as an SR. These techniques not only clean the environment, but also produce valuable H_2 energy. Wide band gap materials can be subjected to band gap engineering to enable activity in the visible light region by doping or creating intrinsic defects. Care should be taken with intrinsic defects as they can act as electron traps, reducing the efficiency of production, whereas hole traps are useful. Defect-mediated catalysis is of prime importance, although these concepts require further investigation.

Delaying the recombination of the photogenerated e–h pairs is the primary objective in enhancing the catalytic activity. The availability of these charge carriers, especially the electrons, on the surface of the catalyst is vital. The transport of electrons to the surface can be improved by creating an internal electric field *via* heterojunctions. The best studied heterojunctions are based on NWs or NRs, which possess the crucial property of vectorial charge transport. Various methods have been used to fabricate these 1D structures, although electrospinning has the most potential because of its versatility in producing such structures.

It is important to consider a semiconductor combination that drives electrons to the surface of the heterocatalyst, while other combinations separate e–h pairs in the background. Such a combination should increase the harvesting of solar energy. For example, $Zn_xCd_{1-x}Te$ in conjunction with ZnO in heterostructures helps to extend the absorption of solar energy into the NIR region, which can be as high as 22% of the solar spectrum.[35]

In the process of fabrication, inorganic nanostructures are generally subjected to thermal treatment(s), note that there are exceptions. Various studies have shown the dependence of H_2 production on processing parameters, such as the calcination temperature. However, excessively high temperatures can decrease the output.[93] The calcination temperature is crucial in determining the quality of the crystal, which, in turn, determines the efficacy of H_2 evolution when balanced against the defect density. The density of defects is also process-dependent. The catalytic activity is related to the number density of active sites, which may not be directly related to the SA measured through N_2 adsorption and desorption curves. Irregularities on the surface may increase the SA; however, the increased area is not necessarily directly correlated with H_2 evolution. For example, H_2 evolution increases with synthesis temperature, although the SA decreases.[229] The characteristic defect density[238–241] may be obtained from photoluminescence measurements. These can be correlated with the photocatalytic

activity[36,172,173] to give a better understanding of the development of promising materials. The photoluminescence may be taken as a standard measurement to quantify the defect density from radiative recombinations. The relation between SA and H_2 evolution has been extensively studied, but a clear correlation has not been obtained because the evolution of H_2 depends on a number of variables, such as the catalyst properties,[276] the particle size,[277] co-catalysts, the SRs, sensitizers[85] and, in particular, the kinetics of the chemical reactions that lead to the final formation of O_2 and H_2.[278]

Finally, the following points need to be considered for the design of efficient and cost-effective photocatalysts: (i) band gap engineering to improve the absorption of photons in the solar spectrum; (ii) an increase in the recombination time of the photogenerated excitons so they can take part in photocatalysis; and (iii) avoidance of back-reactions to form water.

Acknowledgements

V.J.B. and S.V. thank the Scientific & Technological Research Council of Turkey (TUBITAK) (TUBITAK-BIDEB 2221, Fellowships for Visiting Scientists and Scientists on Sabbatical) for fellowship. T.U. thanks EU FP7-Marie Curie-IRG (NANOWEB, PIRG06-GA-2009-256428) and The Turkish Academy of Sciences–Outstanding Young Scientists Award Program (TUBA-GEBIP) for funding.

Notes and references

1 Z. Zou, J. Ye, K. Sayama and H. Arakawa, *Nature*, 2001, **414**, 625–627.
2 M. Ashokkumar, *Int. J. Hydrogen Energy*, 1998, **23**, 427–438.
3 H. Balat and E. Kirtay, *Int. J. Hydrogen Energy*, 2010, **35**, 7416–7426.
4 M. Ni, M. K. H. Leung, D. Y. C. Leung and K. Sumathy, *Renewable Sustainable Energy Rev.*, 2007, **11**, 401–425.
5 K. Shimura and H. Yoshida, *Energy Environ. Sci.*, 2011, **4**, 2467–2481.
6 X. Song and L. Gao, *J. Phys. Chem. C*, 2008, **112**, 15299–15305.
7 F. Lu, W. Cai and Y. Zhang, *Adv. Funct. Mater.*, 2008, **18**, 1047–1056.
8 B. B. Kale, J.-O. Baeg, S. M. Lee, H. Chang, S.-J. Moon and C. W. Lee, *Adv. Funct. Mater.*, 2006, **16**, 1349–1354.
9 W.-T. Yao, S.-H. Yu, S.-J. Liu, J.-P. Chen, X.-M. Liu and F.-Q. Li, *J. Phys. Chem. B*, 2006, **110**, 11704–11710.
10 J. Zhang, F. Shi, J. Lin, D. Chen, J. Gao, Z. Huang, X. Ding and C. Tang, *Chem. Mater.*, 2008, **20**, 2937–2941.
11 J. K. Zhou, L. Lv, J. Yu, H. L. Li, P.-Z. Guo, H. Sun and X. S. Zhao, *J. Phys. Chem. C*, 2008, **112**, 5316–5321.
12 A. Fujishima and K. Honda, *Nature*, 1972, **238**, 37–38.
13 A. J. Bard, *J. Photochem.*, 1979, **10**, 59–75.
14 A. J. Bard, *Science*, 1980, **207**, 139–144.
15 A. J. Bard, *J. Phys. Chem.*, 1982, **86**, 172–177.
16 A. C. Ford, J. C. Ho, Y.-L. Chueh, Y.-C. Tseng, Z. Fan, J. Guo, J. Bokor and A. Javey, *Nano Lett.*, 2009, **9**, 360–365.
17 A. B. F. Martinson, J. E. McGarrah, M. O. K. Parpia and J. T. Hupp, *Phys. Chem. Chem. Phys.*, 2006, **8**, 4655–4659.
18 S. Hernandez, V. Cauda, A. Chiodoni, S. Dallorto, A. Sacco, D. Hidalgo, E. Celasco and C. F. Pirri, *ACS Appl. Mater. Interfaces*, 2014, **6**, 12153–12167.
19 T. B. Singh, F. Meghdadi, S. Günes, N. Marjanovic, G. Horowitz, P. Lang, S. Bauer and N. S. Sariciftci, *Adv. Mater.*, 2005, **17**, 2315–2320.
20 V. Chakrapani, J. Thangala and M. K. Sunkara, *Int. J. Hydrogen Energy*, 2009, **34**, 9050–9059.
21 K. Aryal, B. N. Pantha, J. Li, J. Y. Lin and H. X. Jiang, *Appl. Phys. Lett.*, 2010, **96**, 052110.
22 J. Hensel, G. Wang, Y. Li and J. Z. Zhang, *Nano Lett.*, 2010, **10**, 478–483.
23 Z. G. Yu, C. E. Pryor, W. H. Lau, M. A. Berding and D. B. MacQueen, *J. Phys. Chem. B*, 2005, **109**, 22913–22919.
24 A. Kudo and Y. Misekia, *Chem. Soc. Rev.*, 2009, **38**, 253–278.
25 S. Yan, L. Wan, Z. Li and Z. Zou, *Chem. Commun.*, 2011, **47**, 5632–5634.
26 K. Saito, K. Koga and A. Kudo, *Dalton Trans.*, 2011, **40**, 3909–3913.
27 D. Barreca, P. Fornasiero, A. Gasparotto, V. Gombac, C. Maccato, T. Montini and E. Tondello, *ChemSusChem*, 2009, **2**, 230–233.
28 W. Siripala, A. Ivanovskaya, T. F. Jaramillo, S.-H. Baeck and E. W. McFarland, *Sol. Energy Mater. Sol. Cells*, 2003, **77**, 229–237.
29 X. Zhao, P. Wang and B. Li, *Chem. Commun.*, 2010, **46**, 6768–6770.
30 R. v. d. Krol, Y. Liang and J. Schoonman, *J. Mater. Chem.*, 2008, **18**, 2311–2320.
31 Y. Li and J. Z. Zhang, *Laser Photonics Rev.*, 2010, **4**, 517–528.
32 K. Shankar, J. I. Basham, N. K. Allam, O. K. Varghese, G. K. Mor, X. Feng, M. Paulose, J. A. Seabold, K.-S. Choi and C. A. Grimes, *J. Phys. Chem. C*, 2009, **113**, 6327–6359.
33 M. Paulose, K. Shankar, S. Yoriya, H. E. Prakasam, O. K. Varghese, G. K. Mor, T. A. Latempa, A. Fitzgerald and C. A. Grimes, *J. Phys. Chem. B*, 2006, **110**, 16179–16184.
34 Y. Izumi, T. Itoi, S. Peng, K. Oka and Y. Shibata, *J. Phys. Chem. C*, 2009, **113**, 6706–6718.
35 X. Zhan, Q. Wang, F. Wang, Y. Wang, Z. Wang, J. Cao, M. Safdar and J. He, *ACS Appl. Mater. Interfaces*, 2014, **6**, 2878–2883.
36 F. Kayaci, S. Vempati, C. Ozgit, I. Donmez, N. Biyikli and T. Uyar, *Nanoscale*, 2014, **6**, 5735.
37 R. Sathre, C. D. Scown, W. R. MorrowIII, J. C. Stevens, I. D. Sharp, J. W. AgerIII, K. Walczak, F. A. Houleae and J. B. Greenblatt, *Energy Environ. Sci.*, 2014, **7**, 3264–3278.
38 T. Hisatomi, J. Kubota and K. Domen, *Chem. Soc. Rev.*, 2014, **43**, 7520–7535.
39 M. Zhou, X. W. D. Lou and Y. Xie, *Nano Today*, 2013, **8**, 598–618.
40 G. Wang, Y. Ling, H. Wang, X. Lu and Y. Li, *J. Photochem. Photobiol., C*, 2014, **19**, 35–51.
41 J. Liu, G. Liu, M. Li, W. Shen, Z. Liu, J. Wang, J. Zhao, L. Jiang and Y. Song, *Energy Environ. Sci.*, 2010, **3**, 1503–1506.

42 E. C. Garnett and P. Yang, *J. Am. Chem. Soc.*, 2008, **130**, 9224–9225.
43 L. Tsakalakos, J. Balch, J. Fronheiser, B. A. Korevaar, O. Sulima and J. Rand, *Appl. Phys. Lett.*, 2007, **91**, 233117.
44 J. B. Veluru, K. K. Manippady, M. Rajendiren, K. M. Mya, P. R. Rayavarapu, S. N. Appukuttan and R. Seeram, *Int. J. Hydrogen Energy*, 2013, **38**, 4324–4333.
45 V. J. Babu, M. K. Kumar, A. S. Nair, T. L. Kheng, S. I. Allakhverdiev and S. Ramakrishna, *Int. J. Hydrogen Energy*, 2012, **37**, 8897–8904.
46 I.-S. Cho, S. Lee, J. H. Noh, D. W. Kim, D. K. Lee, H. S. Jung, D.-W. Kim and K. S. Hong, *J. Mater. Chem.*, 2010, **20**, 3979–3983.
47 S. Ikeda, A. Tanaka, K. Shinohara, M. Hara, J. N. Kondo, K.-I. Maruya and K. Domen, *Microporous Mater.*, 1997, **9**, 253–258.
48 M. C. Hidalgo, M. Aguilar, M. Maicu, J. A. Navío and G. Colón, *Catal. Today*, 2007, **129**, 50–58.
49 A. Testino, I. R. Bellobono, V. Buscaglia, C. Canevali, M. D'Arienzo, S. Polizzi, R. Scotti and F. Morazzoni, *J. Am. Chem. Soc.*, 2007, **129**, 3564–3575.
50 A. Datta, A. Priyam, S. N. Bhattacharyya, K. K. Mukherjea and A. Saha, *J. Colloid Interface Sci.*, 2008, **322**, 128–135.
51 S. Y. Chae, M. K. Park, S. K. Lee, T. Y. Kim, S. K. Kim and W. I. Lee, *Chem. Mater.*, 2003, **15**, 3326–3331.
52 G. Liu, C. Sun, H. G. Yang, S. C. Smith, L. Wang, G. Q. M. Lu and H.-M. Cheng, *Chem. Commun.*, 2010, **46**, 755–757.
53 L. Zhang, J. Li, Z. Chen, Y. Tang and Y. Yu, *Appl. Catal., A*, 2006, **299**, 292–297.
54 J. C. Yu, J. Yu, W. Ho and L. Zhang, *Chem. Commun.*, 2001, 1942–1943.
55 T. Park, S. A. Haque, R. J. Potter, A. B. Holmes and J. R. Durrant, *Chem. Commun.*, 2003, 2878–2879.
56 E. C. Garnett, M. L. Brongersma, Y. Cui and M. D. McGehee, *Annu. Rev. Mater. Res.*, 2011, **41**, 269–295.
57 A. I. Hochbaum and P. Yang, *Chem. Rev.*, 2010, **110**, 527–546.
58 R. Yan, D. Gargas and P. Yang, *Nat. Photonics*, 2009, **3**, 569–576.
59 Z. Xiong, M. Zheng, S. Liu, L. Ma and W. Shen, *Nanotechnology*, 2013, **24**, 265402.
60 Y.-J. Lee, D. S. Ruby, D. W. Peters, B. B. McKenzie and J. W. P. Hsu, *Nano Lett.*, 2008, **8**, 1501–1505.
61 Y. B. Tang, Z. H. Chen, H. S. Song, C. S. Lee, H. T. Cong, H. M. Cheng, W. J. Zhang, I. Bell and S. T. Lee, *Nano Lett.*, 2008, **8**, 4191–4195.
62 S. L. Diedenhofen, G. Vecchi, R. E. Algra, A. Hartsuiker, O. L. Muskens, G. Immink, E. P. A. M. Bakkers, W. L. Vos and J. G. m. Rivas, *Adv. Mater.*, 2009, **21**, 973–978.
63 O. L. Muskens, J. G. Rivas, R. E. Algra, E. P. A. M. Bakkers and A. Lagendijk, *Nano Lett.*, 2008, **8**, 2638–2642.
64 L. Hu and G. Chen, *Nano Lett.*, 2007, **7**, 3249–3252.
65 E. Garnett and P. Yang, *Nano Lett.*, 2010, **10**, 1082–1087.
66 K. Peng, Y. Xu, Y. Wu, Y. Yan, S.-T. Lee and J. Zhu, *Small*, 2005, **1**, 1062–1067.
67 K. Zhu, N. R. Neale, A. Miedaner and A. J. Frank, *Nano Lett.*, 2007, **7**, 69–74.
68 H. W. Jeong and H. Park, *Catal. Today*, 2014, **230**, 15–19.
69 J.-Y. Jung, Z. Guo, S.-W. Jee, H.-D. Um, K.-T. Park and J.-H. Lee, *Opt. Express*, 2010, **18**, A286–A292.
70 Z. Fan, R. Kapadia, P. W. Leu, X. Zhang, Y.-L. Chueh, K. Takei, K. Yu, A. Jamshidi, A. A. Rathore, D. J. Ruebusch, M. Wu and A. Javey, *Nano Lett.*, 2010, **10**, 3823–3827.
71 X. Feng, K. Shankar, O. K. Varghese, M. Paulose, T. J. Latempa and C. A. Grimes, *Nano Lett.*, 2008, **8**, 3781–3786.
72 M. Law, L. E. Greene, J. C. Johnson, R. Saykally and P. Yang, *Nat. Mater.*, 2005, **4**, 455–459.
73 E. Enache-Pommer, J. E. Boercker and E. S. Aydil, *Appl. Phys. Lett.*, 2007, **91**, 123116.
74 S. Gubbala, V. Chakrapani, V. Kumar and M. K. Sunkara, *Adv. Funct. Mater.*, 2008, **18**, 2411–2418.
75 M. Law, L. E. Greene, A. Radenovic, T. Kuykendall, J. Liphardt and P. Yang, *J. Phys. Chem. B*, 2006, **110**, 22652–22663.
76 J. Liang, Y. Cao, H. Lin, Z. Zhang, C. Huang and a. X. Wang, *Inorg. Chem.*, 2013, **52**, 6916–6922.
77 M. Yang, Y. Ji, W. Liu, Y. Wang and X. Liu, *RSC Adv.*, 2014, **4**, 15048–15054.
78 Y. Qiu, S.-F. Leung, Q. Zhang, B. Hua, Q. Lin, Z. Wei, K.-H. Tsui, Y. Zhang, S. Yang and Z. Fan, *Nano Lett.*, 2014, **14**, 2123–2129.
79 D. W. Hwang, H. G. Kim, J. Kim, K. Y. Cha, Y. G. Kim and J. S. Lee, *J. Catal.*, 2000, **193**, 40–48.
80 S. Ikeda, M. Hara, J. N. Kondo and K. Domen, *J. Mater. Res.*, 1998, **13**, 852–855.
81 H. Zhou, X. Li, T. Fan, F. E. Osterloh, J. Ding, E. M. Sabio, D. Zhang and Q. Guo, *Adv. Mater.*, 2010, **22**, 951–956.
82 Z. Liu, D. D. Sun, P. Guo and J. O. Leckie, *Nano Lett.*, 2007, **7**, 1081–1085.
83 G. Yang, W. Yan, Q. Zhang, S. Shen and S. Ding, *Nanoscale*, 2013, **5**, 12432–12439.
84 N. Buhler, K. Meier and J.-F. Reber, *J. Phys. Chem.*, 1984, **88**, 3261–3268.
85 S. K. Choi, S. Kim, J. Ryu, S. K. Lim and H. Park, *Photochem. Photobiol. Sci.*, 2012, **11**, 1437–1444.
86 I. E. Castelli, J. M. G. Lastra, F. Huser, K. S. Thygesen and K. W. Jacobsen, *New J. Phys.*, 2013, **15**, 105026.
87 Y. Xu and M. A. A. Schoonen, *Am. Mineral.*, 2000, **85**, 543–556.
88 J. Zhang, J. Yu, Y. Zhang, Q. Li and J. R. Gong, *Nano Lett.*, 2011, **11**, 4774–4779.
89 I. Gorczyca, T. Suski, N. E. Christensen and A. Svane, *Appl. Phys. Lett.*, 2010, **96**, 101907.
90 S. Burnside, J.-E. Moser, K. Brooks and M. Grätzel, *J. Phys. Chem. B*, 1999, **103**, 9328–9332.
91 S.-C. Chiu and Y.-Y. Li, *J. Cryst. Growth*, 2009, **311**, 1036–1041.
92 T. A. Kandiel, A. Feldhoff, L. Robben, R. Dillert and D. W. Bahnemann, *Chem. Mater.*, 2010, **22**, 2050–2060.
93 J. Jitputti, Y. Suzuki and S. Yoshikawa, *Catal. Commun.*, 2008, **9**, 1265–1271.
94 L. Kavan, M. Gratzel, S. E. Gilbert, C. Klemenz and H. J. Scheel, *J. Am. Chem. Soc.*, 1996, **118**, 6716–6723.
95 B. Ohtani, Y. Ogawa and S.-I. Nishimoto, *J. Phys. Chem. B*, 1997, **101**, 3746–3752.

96 H. Kominami, Y. Ishii, M. Kohno, S. Konishi, Y. Kera and B. Ohtani, *Catal. Lett.*, 2003, **91**, 41–47.
97 L. Yan, J. Zhang, X. Zhou, X. Wu, J. Lan, Y. Wang, G. Liu, J. Yu and L. Zhi, *Int. J. Hydrogen Energy*, 2013, **38**, 3554–3561.
98 S. E. Braslavsky, A. M. Braun, A. E. Cassano, A. V. Emeline, M. I. Litter, L. Palmisano, V. N. Parmon and N. Serpone, *Pure Appl. Chem.*, 2011, **83**, 931–1014.
99 X. Chen and S. S. Mao, *Chem. Rev.*, 2007, **107**, 2891–2959.
100 Y. Lee, T. Watanabe, T. Takata, M. Hara, M. Yoshimura and K. Domen, *Bull. Chem. Soc. Jpn.*, 2007, **80**, 423–428.
101 Z. Zhang, C.-C. Wang, R. Zakaria and J. Y. Ying, *J. Phys. Chem. B*, 1998, **102**, 10871–10878.
102 W. Sun, S. Zhang, Z. Liu, C. Wang and Z. Mao, *Int. J. Hydrogen Energy*, 2008, **33**, 1112–1117.
103 P. V. Kamat, *J. Phys. Chem. C*, 2007, **111**, 2834–2860.
104 N. Bao, L. Shen, T. Takata, D. Lu and K. Domen, *Chem. Lett.*, 2006, **35**, 318–319.
105 H. Liu, J. Yang, J. Liang, Y. Huang and C. Tang, *J. Am. Ceram. Soc.*, 2008, **91**, 1287–1291.
106 J. S. Jang, S. H. Choi, D. H. Kim, J. W. Jang, K. S. Lee and J. S. Lee, *J. Phys. Chem. C*, 2009, **113**, 8990–8996.
107 J. Jitputti, S. Pavasupree, Y. Suzuki and S. Yoshikawa, *Jpn. J. Appl. Phys.*, 2008, **47**, 751–756.
108 Z. Jiang, F. Yang, N. Luo, B. T. T. Chu, D. Sun, H. Shi, T. Xiao and P. P. Edwards, *Chem. Commun.*, 2008, 6372–6374.
109 S. Palmas, A. M. Polcaro, J. R. Ruiz, A. D. Pozzo, M. Mascia and A. Vacca, *Int. J. Hydrogen Energy*, 2010, **35**, 6561–6570.
110 J. Yu, H. Yu, B. Cheng and C. Trapalis, *J. Mol. Catal. A: Chem.*, 2006, **249**, 135–142.
111 H. Jia, W.-J. Xiao, L. Zhang, Z. Zheng, H. Zhang and F. Deng, *J. Phys. Chem. C*, 2008, **112**, 11379–11384.
112 Y. Wang, L. Zhang, K. Deng, X. Chen and Z. Zou, *J. Phys. Chem. C*, 2007, **111**, 2709–2714.
113 Y. Li, Y. Hu, S. Peng, G. Lu and S. Li, *J. Phys. Chem. C*, 2009, **113**, 9352–9358.
114 Y. Li, T. Sasaki, Y. Shimizu and N. Koshizaki, *J. Am. Chem. Soc.*, 2008, **130**, 14755–14762.
115 F. A. Frame, E. C. Carroll, D. S. Larsen, M. Sarahan, N. D. Browning and F. E. Osterloh, *Chem. Commun.*, 2008, 2206–2208.
116 D. Chen and J. Ye, *Chem. Mater.*, 2009, **21**, 2327–2333.
117 S. Chuangchote, J. Jitputti, T. Sagawa and S. Yoshikawa, *ACS Appl. Mater. Interfaces*, 2009, **1**, 1140–1143.
118 Z. Zhang, Z. Wang, S.-W. Cao and C. Xue, *J. Phys. Chem. C*, 2013, **117**, 25939–25947.
119 S. S. Lee, H. Bai, Z. Liu and D. D. Sun, *Int. J. Hydrogen Energy*, 2012, **37**, 10575–10584.
120 L. Macaraig, S. Chuangchote and T. Sagawa, *J. Mater. Res.*, 2014, **29**, 123–130.
121 H. Bai, Z. Liu and D. D. Sun, *J. Am. Ceram. Soc.*, 2013, **96**, 942–949.
122 X. Yang, A. Wolcott, G. Wang, A. Sobo, R. C. Fitzmorris, F. Qian, J. Z. Zhang and Y. Li, *Nano Lett.*, 2009, **9**, 2331–2336.
123 J. Jitputti, S. Pavasupree, Y. Suzuki and S. Yoshikawa, *J. Solid State Chem.*, 2007, **180**, 1743–1749.
124 A. Patsoura, D. I. Kondarides and X. E. Verykios, *Catal. Today*, 2007, **124**, 94–102.
125 A. Galińska and J. Walendziewski, *Energy Fuels*, 2005, **19**, 1143–1147.
126 P. Tongying, F. Vietmeyer, D. Aleksiuk, G. J. Ferraudi, G. Krylova and M. Kuno, *Nanoscale*, 2014, **6**, 4117–4124.
127 M.-C. Wu, J. Hiltunen, A. Sapi, A. Avila, W. Larsson, H.-C. Liao, M. Huuhtanen, G. Toth, A. Shchukarev, N. Laufer, A. Kukovecz, Z. Konya, J.-P. Mikkola, R. Keiski, W.-F. Su, Y.-F. Chen, H. Jantunen, P. M. Ajayan, R. Vajtai and K. Kordas, *ACS Nano*, 2011, **5**, 5025–5030.
128 G. K. Mor, H. E. Prakasam, O. K. Varghese, K. Shankar and C. A. Grimes, *Nano Lett.*, 2007, **7**, 2356–2364.
129 G. K. Mor, K. Shankar, M. Paulose, O. K. Varghese and C. A. Grimes, *Nano Lett.*, 2005, **5**, 191–195.
130 O. K. Varghese, M. Paulose, K. Shankar, G. K. Mor and C. A. Grimes, *J. Nanosci. Nanotechnol.*, 2005, **5**, 1158–1165.
131 K. Shankar, G. K. Mor, H. E. Prakasam, S. Yoriya, M. Paulose, O. K. Varghese and C. A. Grimes, *Nanotechnology*, 2007, **18**, 065707.
132 G. K. Mor, O. K. Varghese, R. H. T. Wilke, S. Sharma, K. Shankar, T. J. Latempa, K.-S. Choi and C. A. Grimes, *Nano Lett.*, 2008, **8**, 1906–1911.
133 D. Eder, M. Motta and A. H. Windle, *Nanotechnology*, 2009, **20**, 055602.
134 J. H. Park, S. Kim and A. J. Bard, *Nano Lett.*, 2006, **6**, 24–28.
135 W. H. Lubberhuizen, D. Vanmaekelbergh and E. V. Faassen, *J. Porous Mater.*, 2000, **7**, 147–152.
136 A. F. Feil, P. Migowski, F. R. Scheffer, M. D. Pierozan, R. R. Corsetti, M. Rodrigues, R. P. Pezzi, G. Machado, L. Amaral, S. R. Teixeira, D. E. Weibel and J. Dupont, *J. Braz. Chem. Soc.*, 2010, **21**, 1359–1365.
137 Y.-C. Pu, G. Wang, K.-D. Chang, Y. Ling, Y.-K. Lin, B. C. Fitzmorris, C.-M. Liu, X. Lu, Y. Tong, J. Z. Zhang, Y.-J. Hsu and Y. Li, *Nano Lett.*, 2013, **13**, 3817–3823.
138 A. Wood, M. Giersig and P. Mulvaney, *J. Phys. Chem. B*, 2001, **105**, 8810–8815.
139 T.-C. Pan, S.-H. Wang, Y.-S. Lai, J.-M. Jehng and S.-J. Huang, *Appl. Surf. Sci.*, 2014, **296**, 189–194.
140 M. Ye, J. Gong, Y. Lai, C. Lin and Z. Lin, *J. Am. Chem. Soc.*, 2012, **134**, 15720–15723.
141 F.-C. Wang, C.-H. Liu, C.-W. Liu, J.-H. Chao and C.-H. Lin, *J. Phys. Chem. C*, 2009, **113**, 13832–13840.
142 R. P. Antony, T. Mathews, C. Ramesh, N. Murugesan, A. Dasgupta, S. Dhara, S. Dash and A. K. Tyagi, *Int. J. Hydrogen Energy*, 2012, **37**, 8268–8276.
143 X. Wang, G. Liu, Z.-G. Chen, F. Li, G. Q. M. Lu and H.-M. Cheng, *Electrochem. Commun.*, 2009, 1174–1178.
144 M. P. Languer, F. R. Scheffer, A. F. Feil, D. L. Baptista, P. Migowski, G. J. Machado, D. P. d. Moraes, J. Dupont, S. R. Teixeira and D. E. Weibel, *Int. J. Hydrogen Energy*, 2013, **38**, 14440–14450.
145 Y. Li, H. Yu, C. Zhang, W. Song, G. Li, Z. Shao and B. Yi, *Electrochim. Acta*, 2013, **107**, 313–319.

146 J. Gong, Y. Lai and C. Lin, *Electrochim. Acta*, 2010, **55**, 4776–4782.
147 J. Gong, W. Pu, C. Yang and J. Zhang, *Catal. Commun.*, 2013, **36**, 89–93.
148 R. V. Gonçalves, P. Migowski, H. Wender, D. Eberhardt, D. E. Weibel, F. v. C. Sonaglio, M. J. M. Zapata, J. Dupont, A. F. Feil and S. R. Teixeira, *J. Phys. Chem. C*, 2012, **116**, 14022–14030.
149 M. Cargnello, M. Grzelczak, B. Rodriguez-Gonzalez, Z. Syrgiannis, K. Bakhmutsky, V. L. Parola, L. M. Liz-Marzan, R. J. Gorte, M. Prato and P. Fornasiero, *J. Am. Chem. Soc.*, 2012, **134**, 11760–11766.
150 X. Chen and A. Selloni, *Chem. Rev.*, 2014, **114**, 9281–9282.
151 Y. Lee, T. Watanabe, T. Takata, M. Hara, M. Yoshimura and K. Domen, *Bull. Chem. Soc. Jpn.*, 2007, **80**, 423–428.
152 H. Bai, Z. Liu and D. D. Sun, *J. Mater. Chem.*, 2012, **22**, 18801–18807.
153 B. M. Kayes, H. A. Atwater and N. S. Lewis, *J. Appl. Phys.*, 2005, **97**, 114302.
154 D. Chen and J. Ye, *Chem. Mater.*, 2007, **19**, 4585–4591.
155 Y. Sun, W. D. Chemelewski, S. P. Berglund, C. Li, H. He, G. Shi and C. B. Mullins, *ACS Appl. Mater. Interfaces*, 2014, **6**, 5494–5499.
156 B. Sun, T. Shi, Z. Peng, W. Sheng, T. Jiang and G. Liao, *Nanoscale Res. Lett.*, 2013, **8**, 462.
157 K. Lin, B. Ma, W. Su and W. Liu, *Appl. Surf. Sci.*, 2013, **286**, 61–65.
158 J. Liang, J. Xu, Q. Gu, Y. Zhou, C. Huang, H. Lin and X. Wang, *J. Mater. Chem. A*, 2013, **1**, 7798–7805.
159 X. Yang, J. Xu, T. Wong, Q. Yang and C.-S. Lee, *Phys. Chem. Chem. Phys.*, 2013, **15**, 12688–12693.
160 D. Li and Y. Xia, *Adv. Mater.*, 2004, **16**, 1151–1170.
161 A. Greiner and J. H. Wendorff, *Angew. Chem., Int. Ed.*, 2007, **46**, 5670–5703.
162 D. H. Reneker and A. L. Yarin, *Polymer*, 2008, **49**, 2387–2425.
163 X. Lu and C. W. a. Y. Wei, *Small*, 2009, **5**, 2349–2370.
164 S. J. Limmer, *Adv. Mater.*, 2003, **15**, 427–431.
165 Z. Miao, D. Xu, J. Ouyang, G. Guo, X. Zhao and Y. Tang, *Nano Lett.*, 2002, **2**, 717–720.
166 M. Adachi, Y. Murata, J. Takao, J. Jiu, M. Sakamoto and F. Wang, *J. Am. Chem. Soc.*, 2004, **126**, 14943–14949.
167 Y.-w. Jun, M. F. Casula, J.-H. Sim, S. Y. Kim, J. Cheon and A. P. Alivisatos, *J. Am. Chem. Soc.*, 2003, **125**, 15981–15985.
168 J.-M. Wu, H. C. Shih and W.-T. Wu, *Nanotechnology*, 2006, **17**, 105–109.
169 Z. R. Tian, J. A. Voigt, J. Liu, B. Mckenzie and H. Xu, *J. Am. Chem. Soc.*, 2003, **125**, 12384–12385.
170 V. S. P. Kumar, V. J. Babu, G. K. Raghuraman, R. Dhamodharan and T. S. Natarajan, *J. Appl. Phys.*, 2007, **101**, 114317.
171 V. J. Babu, S. Vempati and S. Ramakrishna, *RSC Adv.*, 2014, **4**, 27979–27987.
172 F. Kayaci, S. Vempati, I. Donmez, N. Biyikli and T. Uyar, *Nanoscale*, 2014, **6**, 10224–10234.
173 F. Kayaci, S. Vempati, C. O. Akgun, N. Biyikli and T. Uyar, *Appl. Catal., B*, 2014, **156–157**, 173–183.
174 V. J. Babu, R. S. R. Bhavatharini and S. Ramakrishna, *RSC Adv.*, 2014, **4**, 29957–29963.
175 M. M. Khin, S. Nair, J. B. Veluru, M. Rajendiran and S. Ramakrishna, *Energy Environ. Sci.*, 2012, **5**, 8075–8109.
176 V. J. Babu, S. Vempati, S. Sundarrajan, M. Sireesha and S. Ramakrishna, *Sol. Energy*, 2014, **106**, 1–22.
177 Y.-Z. Long, M. Yu, B. Sun, C.-Z. Gu and Z. Fan, *Chem. Soc. Rev.*, 2012, **41**, 4560–4580.
178 C. J. Luo, S. D. Stoyanov, E. Stride, E. Pelan and M. Edirisinghe, *Chem. Soc. Rev.*, 2012, **41**, 4708–4735.
179 A. A. Madhavan, S. Kalluri, D. K. Chacko, T. A. Arun, S. Nagarajan, K. R. V. Subramanian, A. S. Nair, S. V. Nair and A. Balakrishnan, *RSC Adv.*, 2012, **2**, 13032–13037.
180 G. Dong, X. Xiao, L. Zhang, Z. Ma, X. Bao, M. Peng, Q. Zhang and J. Qiu, *J. Mater. Chem.*, 2011, **21**, 2194–2203.
181 A. Babel, D. Li, Y. Xia and S. A. Jenekhe, *Macromolecules*, 2005, **38**, 4705–4711.
182 M. Tanveer, A. Habib and M. B. Khan, *J. Exp. Nanosci.*, 2014, DOI: 10.1080/17458080.2013.869841.
183 P. Ahmadpoor, A. S. Nateri and V. Motaghitalab, *J. Appl. Polym. Sci.*, 2013, **130**, 78–85.
184 L. Gao and C. Li, *J. Lumin.*, 2010, **130**, 236–239.
185 M. A. Kanjwal, N. A. M. Barakat, F. A. Sheikh, D. K. Park and H. Y. Kim, *J. Mater. Sci.*, 2010, **45**, 3833–3840.
186 J. B. Veluru, K. K. Satheesh, D. C. Trivedi, M. V. Ramakrishna and T. N. Srinivasan, *J. Eng. Fibers Fabr.*, 2007, **2**, 25.
187 S. Vempati, J. B. Veluru, R. G. Karunakaran, D. Raghavachari and T. S. Natarajan, *J. Appl. Phys.*, 2011, **110**, 113718.
188 M. M. Munir, F. Iskandar, K. M. Yun, K. Okuyama and M. Abdullah, *Nanotechnology*, 2008, **19**, 145603.
189 J.-Y. Chen, C.-C. Kuo, C.-S. Lai, W.-C. Chen and H.-L. Chen, *Macromolecules*, 2011, **44**, 2883–2892.
190 C. Drew, X. Liu, D. Ziegler, X. Wang, F. F. Bruno, J. Whitten, L. A. Samuelson and J. Kumar, *Nano Lett.*, 2003, **3**, 143–147.
191 B. Ding, M. Wang, J. Yu and G. Sun, *Sensors*, 2009, **9**, 1609–1624.
192 H. Wu, L. Hu, M. W. Rowell, D. Kong, J. J. Cha, J. R. McDonough, J. Zhu, Y. Yang, M. D. McGehee and Y. Cui, *Nano Lett.*, 2010, **10**, 4242–4248.
193 Y. Shmueli, G. E. Shter, O. Assad, H. Haick, P. Sonntag, P. Ricoux and G. S. Grader, *J. Mater. Res.*, 2012, **27**, 1672–1679.
194 A. Kumar, R. Jose, K. Fujihara, J. Wang and S. Ramakrishna, *Chem. Mater.*, 2007, **19**, 6536–6542.
195 D. Hou, X. Hu, Y. Wen, B. Shan, P. Hu, X. Xiong, Y. Qiao and Y. Huang, *Phys. Chem. Chem. Phys.*, 2013, **15**, 20698–20705.
196 V. J. Babu, S. Vempati, G. J. Subha, V. Kumari, T. S. Natarajan, A. S. Nair and S. Ramakrishna, *J. Eng. Fibers Fabr.*, 2011, **6**, 57–59.
197 V. J. Babu, V. S. P. Kumar, B. Sundaray, V. R. K. Murthy and T. S. Natarjan, *Mater. Sci. Eng., B*, 2007, **142**, 46–50.
198 H. Bai, J. Juay, Z. Liu, X. Song, S. S. Lee and D. D. Sun, *Appl. Catal., B*, 2012, **125**, 367–374.
199 T. Sun, J. Qiu and C. Liang, *J. Phys. Chem. C*, 2008, **112**, 715–721.
200 W.-W. Wang, Y.-J. Zhu and L.-X. Yang, *Adv. Funct. Mater.*, 2007, **17**, 59–64.

201 S. Xiong, B. Xi, C. Wang, G. Xi and X. L. a. Y. Qian, *Chem. – Eur. J.*, 2007, **13**, 7926–7932.
202 T.-G. Xu, C. Zhang, X. Shao, K. Wu and Y.-F. Zhu, *Adv. Funct. Mater.*, 2006, **16**, 1599–1607.
203 Y. Matsumoto, S. Ida and T. Inoue, *J. Phys. Chem. C*, 2008, **112**, 11614–11616.
204 E. C. Carroll, O. C. Compton, D. Madsen, F. E. Osterloh and D. S. Larsen, *J. Phys. Chem. C*, 2008, **112**, 2394–2403.
205 C. Ye, Y. Bando, G. Shen and D. Golberg, *J. Phys. Chem. B*, 2006, **110**, 15146–15151.
206 C. Zhang and Y. Zhu, *Chem. Mater.*, 2005, **17**, 3537–3545.
207 V. J. Babu, S. R. S. Bhavatharini and S. Ramakrishna, *RSC Adv.*, 2014, **4**, 19251–19256.
208 S. H. Kim, S. Park, C. W. Lee, B. S. Han, S. W. Seo, J. S. Kim, I. S. Cho and K. S. Hong, *Int. J. Hydrogen Energy*, 2012, **37**, 16895–16902.
209 K. Parida, M. Satpathy and L. Mohapatra, *J. Mater. Chem.*, 2012, **22**, 7350–7357.
210 L. Zhao, J. Ran, Z. Shu, G. Dai, P. Zhai and S. Wang, *Int. J. Photoenergy*, 2012, **2012**, 472958.
211 Z. Li, J. Shen, J.-Q. Wang, D. Wang, Y. Huang and J. Zou, *CrystEngComm*, 2012, **14**, 1874–1880.
212 O. C. Compton and F. E. Osterloh, *J. Phys. Chem. C*, 2009, **113**, 479–485.
213 M. Harada, T. Sasaki, Y. Ebina and M. Watanabe, *J. Photochem. Photobiol., A*, 2002, **148**, 273–276.
214 L. Zhang, D. Chen and X. Jiao, *J. Phys. Chem. B*, 2006, **110**, 2668–2673.
215 X. Zhang, Z. Ai, F. Jia and L. Zhang, *J. Phys. Chem. C*, 2008, **112**, 747–753.
216 M. C. Sarahan, E. C. Carroll, M. Allen, D. S. Larsen, N. D. Browning and F. E. Osterloh, *J. Solid State Chem.*, 2008, **181**, 1678–1683.
217 J. Yu, L. Qi and M. Jaroniec, *J. Phys. Chem. C*, 2010, **114**, 13118–13125.
218 G. Xiang, T. Li, J. Zhuang and X. Wang, *Chem. Commun.*, 2010, **46**, 6801–6803.
219 J. Jitputti, T. Rattanavoravipa, S. Chuangchote, S. Pavasupree, Y. Suzuki and S. Yoshikawa, *Catal. Commun.*, 2009, **10**, 378–382.
220 O. C. Compton, E. C. Carroll, J. Y. Kim, D. S. Larsen and F. E. Osterloh, *J. Phys. Chem. C*, 2007, **111**, 14589–14592.
221 O. C. Compton, C. H. Mullet, S. Chiang and F. E. Osterloh, *J. Phys. Chem. C*, 2008, **112**, 6202–6208.
222 X. Chen, S. Shen, L. Guo and S. S. Mao, *Chem. Rev.*, 2010, **110**, 6503–6570.
223 M. Machida, X. W. Ma, H. Taniguchi, J.-I. Yabunaka and T. Kijima, *J. Mol. Catal. A: Chem.*, 2000, **155**, 131–142.
224 T. Sasaki, *J. Ceram. Soc. Jpn.*, 2007, **115**, 9–16.
225 T. Yamase, *Chem. Rev.*, 1998, **98**, 307–326.
226 E. M. Sabio, R. L. Chamousis, N. D. Browning and F. E. Osterloh, *J. Phys. Chem. C*, 2012, **116**, 3161–3170.
227 Y. Zhang, T. Xia, M. Shang, P. Wallenmeyer, D. Katelyn, A. Peterson, J. Murowchick, L. Dong and X. Chen, *RSC Adv.*, 2014, **4**, 16146–16152.
228 S. S. Lee, H. Bai, Z. Liu and D. D. Sun, *Water Res.*, 2013, **47**, 4059–4073.
229 J. S. Jang, U. A. Joshi and J. S. Lee, *J. Phys. Chem. C*, 2007, **111**, 13280–13287.
230 J. Zhang, Y. Wang, J. Jin, J. Zhang, Z. Lin, F. Huang and J. Yu, *ACS Appl. Mater. Interfaces*, 2013, **5**, 10317–10324.
231 Q. Li and G. Lu, *J. Power Sources*, 2008, **185**, 577–583.
232 M. G. Kibria, S. Zhao, F. A. Chowdhury, Q. Wang, H. P. T. Nguyen, M. L. Trudeau, H. Guo and Z. Mi, *Nat. Commun.*, 2014, **5**, 3825.
233 C. Li, J. Yuan, B. Han, L. Jiang and W. Shangguan, *Int. J. Hydrogen Energy*, 2010, **35**, 7073–7079.
234 C. Liu, J. Tang, H. M. Chen, B. Liu and P. Yang, *Nano Lett.*, 2013, **13**, 2989–2992.
235 M. G. Kibria, H. P. T. Nguyen, K. Cui, S. Zhao, D. Liu, H. Guo, M. L. Trudeau, S. Paradis, A.-R. Hakima and Z. Mi, *ACS Nano*, 2013, **7**, 7886–7893.
236 K. Maeda, N. Sakamoto, T. Ikeda, H. Ohtsuka, A. Xiong, D. Lu, M. Kanehara, T. Teranishi and K. Domen, *Chem. – Eur. J.*, 2010, **16**, 7750–7759.
237 B. AlOtaibi, H. P. T. Nguyen, S. Zhao, M. G. Kibria, S. Fan and Z. Mi, *Nano Lett.*, 2013, **13**, 4356–4361.
238 S. Vempati, S. Chirakkara, J. Mitra, P. Dawson, K. K. Nanda and S. B. Krupanidhi, *Appl. Phys. Lett.*, 2012, **100**, 162104.
239 S. Vempati, J. Mitra and P. Dawson, *Nanoscale Res. Lett.*, 2012, **7**, 470.
240 S. Vempati, A. Shetty, P. Dawson, K. Nanda and S. B. Krupanidhi, *J. Cryst. Growth*, 2012, **343**, 7–12.
241 S. Vempati, A. Shetty, P. Dawson, K. K. Nanda and S. B. Krupanidhi, *Thin Solid Films*, 2012, **524**, 137–143.
242 Q. Kang, J. Cao, Y. Zhang, L. Liu, H. Xu and J. Ye, *J. Mater. Chem. A*, 2013, **1**, 5766–5774.
243 Y. Liu, H. Zhou, B. Zhou, J. Li, H. Chen, J. Wang, J. Bai, W. Shangguan and W. Cai, *Int. J. Hydrogen Energy*, 2011, **36**, 167–174.
244 Q. Li and G. Lu, *J. Mol. Catal. A: Chem.*, 2007, **266**, 75–79.
245 Q. Li, L. Chen and G. Lu, *J. Phys. Chem. C*, 2007, **111**, 11494–11499.
246 G. Khan, S. K. Choi, S. Kim, S. K. Lim, J. S. Jang and H. Park, *Appl. Catal., B*, 2013, **142–143**, 647–653.
247 S. K. Parayil, J. Baltrusaitis, C.-M. Wu and R. T. Koodali, *Int. J. Hydrogen Energy*, 2013, **38**, 2656–2669.
248 P. Khemthong, P. Photai and N. Grisdanurak, *Int. J. Hydrogen Energy*, 2013, **38**, 15992–16001.
249 J. Ran, J. Yu and M. Jaroniec, *Green Chem.*, 2011, **13**, 2708–2713.
250 N. S. Chaudhari, S. S. Warule, S. Muduli, B. B. Kale, S. Jouen, B. Lefez, B. Hannoyer and S. B. Ogale, *Dalton Trans.*, 2011, **40**, 8003–8011.
251 H. Lv, L. Ma, P. Zeng, D. Ke and T. Peng, *J. Mater. Chem.*, 2010, **20**, 3665–3672.
252 S. Mubeen, J. Lee, N. Singh, S. Krämer, G. D. Stucky and M. Moskovits, *Nat. Nanotechnol.*, 2013, **8**, 247–251.
253 S. S. Lee, H. Bai, Z. Liu and D. D. Sun, *Appl. Catal., B*, 2013, **140**, 68–81.
254 Z. Zhang, A. Li, S.-W. Cao, M. Bosman, S. Li and C. Xue, *Nanoscale*, 2014, **6**, 5217–5222.

255 A. Yousef, N. A. M. Barakat, K. A. Khalil, A. R. Unnithan, G. Panthi, B. Pant and H. Y. Kim, *Colloids Surf., A*, 2012, **410**, 59–65.
256 N. Sobti, A. Bensouici, F. Coloma, C. Untiedt and S. Achour, *J. Nanopart. Res.*, 2014, **16**, 2577.
257 A. R. Unnithan, N. A. M. Barakat, R. Nirmala, S. S. Al-Deyab and H. Y. Kim, *Ceram. Int.*, 2012, **38**, 5175–5180.
258 Q. Li, X. Sun, K. Lozano and Y. Mao, *J. Phys. Chem. C*, 2014, **118**, 13467–13475.
259 N. Bao, L. Shen, T. Takata and K. Domen, *Chem. Mater.*, 2008, **20**, 110–117.
260 Z. Lei, W. You, M. Liu, G. Zhou, T. Takata, M. Hara, K. Domen and C. Li, *Chem. Commun.*, 2003, 2142–2143.
261 S. Siol, H. Strater, R. Bruggemann, J. Brotz, G. H. Bauer, A. Klein and W. Jaegermann, *J. Phys. D: Appl. Phys.*, 2013, **46**, 495112.
262 X. Li, H. Shen, S. Li, J. Z. Niu, H. Wang and L. S. Li, *J. Mater. Chem.*, 2010, **20**, 923–928.
263 S. Panigrahi and D. Basak, *RSC Adv.*, 2012, **2**, 11963–11968.
264 Z. Khan, M. Khannam, N. Vinothkumar, M. De and M. Qureshi, *J. Mater. Chem.*, 2012, **22**, 12090–12095.
265 Q. Li, B. Guo, J. Yu, J. Ran, B. Zhang, H. Yan and J. R. Gong, *J. Am. Chem. Soc.*, 2011, **133**, 10878–10884.
266 Y. Li, Y.-L. Li, C. M. Araujo, W. Luo and R. Ahuja, *Catal. Sci. Technol.*, 2013, **3**, 2214–2220.
267 Z. Xu, Y. Li, S. Peng, G. Lu and S. Li, *RSC Adv.*, 2012, **2**, 3458–3466.
268 X. Bai and J. Li, *Mater. Res. Bull.*, 2012, **46**, 1028–1034.
269 F. A. Frame and F. E. Osterloh, *J. Phys. Chem. C*, 2010, **114**, 10628–10633.
270 X. Wang, K. Maeda, A. Thomas, K. Takanabe, G. Xin, J. M. Carlsson, K. Domen and M. Antonietti, *Nat. Mater.*, 2008, **8**, 76–80.
271 X. Wang, K. Maeda, X. Chen, K. Takanabe, K. Domen, Y. Hou, X. Fu and M. Antonietti, *J. Am. Chem. Soc.*, 2009, **131**, 1680–1681.
272 J. Liu, J. Huang, H. Zhou and M. Antonietti, *ACS Appl. Mater. Interfaces*, 2014, **6**, 8434–8440.
273 J. Huang, M. Antonietti and J. Liu, *J. Mater. Chem. A*, 2014, **2**, 7686–7693.
274 A. Yousef, N. A. M. Barakat and H. Y. Kim, *Appl. Catal., A*, 2013, **467**, 98–106.
275 http://energy.gov/eere/fuelcells/market-analysis-reports.
276 K. Maeda, H. Hashiguchi, H. Masuda, R. Abe and K. Domen, *J. Phys. Chem. C*, 2008, **112**, 3447–3452.
277 K. Nishijima, T. Kamai, N. Murakami, T. Tsubota and T. Ohno, *Int. J. Photoenergy*, 2008, 173943.
278 J. Tang, J. R. Durrant and D. R. Klug, *J. Am. Chem. Soc.*, 2008, **130**, 13885–13891.

